RESEARCH ARTICLE SUMMARY

INNATE IMMUNITY

Mammalian lipid droplets are innate immune hubs integrating cell metabolism and host defense

Marta Bosch*†, Miguel Sánchez-Álvarez†, Alba Fajardo, Ronan Kapetanovic, Bernhard Steiner, Filipe Dutra, Luciana Moreira, Juan Antonio López, Rocío Campo, Montserrat Marí, Frederic Morales-Paytuví, Olivia Tort, Albert Gubern, Rachel M. Templin, James E. B. Curson, Nick Martel, Cristina Català, Francisco Lozano, Francesc Tebar, Carlos Enrich, Jesús Vázquez, Miguel A. Del Pozo, Matthew J. Sweet, Patricia T. Bozza, Steven P. Gross, Robert G. Parton*, Albert Pol*

INTRODUCTION: In all eukaryotic cells, lipid droplets (LDs) store and supply essential lipids to produce signaling molecules, membrane building blocks, and metabolic energy. The LD monolayer also accommodates proteins not obviously related to lipids, such as transcription factors, chromatin components, and toxic proteins.

Common parasites (such as trypanosomes and *Plasmodium falciparum*), bacteria (such as mycobacteria and *Chlamydia*), and viruses (such as hepatitis C and dengue) induce and target LDs during their life cycles. The current view is that LDs support infection, providing microorganisms with substrates for effective growth.

RATIONALE: Successful innate defense is critical for survival, and host species have efficiently coevolved with pathogens to develop a plethora of immune responses. Multiple cues, including cellular stress and danger-associated molecular patterns such as lipopolysaccharide (LPS), induce LD formation. Thus, LD localization and dynamics may potentially be advantageous for organizing an intracellular host defense. We have investigated the possibility that mammalian LDs have a direct and regulated role in innate immunity.

RESULTS: We show that mammalian LDs are endowed with a protein-mediated antimicrobial capacity, which is up-regulated during polymicrobial sepsis and by LPS. Light and electron microscopy demonstrated specific association of LDs and bacteria in human macrophages, suggesting the existence of docking mechanisms that facilitate the engagement of antibacterial LD proteins with bacteria.

A comparative mass spectrometry profiling of proteins differentially associated with LDs in response to LPS (LPS-LDs) revealed the profound remodeling of the organelle proteome. A stringent evaluation identified 689 proteins differentially regulated on LPS-LDs (317 enriched and 372 reduced). Ingenuity Pathway Analysis revealed an enrichment of innate immune system–related components and reduction of metabolism-related LD-resident proteins. Additional analyses suggested that LDs serve as innate immune hubs, integrating major intra- and extracellular immune responses.

Among the five members of the perilipin family of LD surface proteins (PLINs), PLIN5 was the only one down-regulated on LPS-LDs. PLIN5 reduction promoted physical and functional disconnection of LPS-LDs and mitochondria, with a concomitant reduction of oxidative metabolism and ketogenesis. Forced PLIN5 reexpression increased the number of LD-mitochondria contacts, reducing LD-bacteria interactions and compromising the antimicrobial capacity of cells.

By contrast, PLIN2 was the most up-regulated PLIN on LPS-LDs. Gene interaction analysis revealed that multiple immune proteins nucleated around PLIN2 in response to LPS. LPS-LDs accrued several interferon-inducible proteins such as viperin, IGTP, IIGP1, TGTP1, and IFI47. Furthermore, LPS-LDs also accumulated cathelicidin (CAMP), a broad-spectrum antimicrobial peptide with chemotactic properties. Cells overexpressing a LD-associated CAMP were more resistant to different bacterial species, including *Escherichia coli*, methicillin-resistant *Staphylococcus aureus*, and *Listeria monocytogenes*.

CONCLUSION: These results demonstrate that LDs form a first-line intracellular defense. They act as a molecular switch in innate immunity, responding to danger signals by both reprogramming cell metabolism and eliciting protein-mediated antimicrobial mechanisms. Mechanisms of LD trafficking and docking with phagocytic and parasitophorous membranes, observed here and described for several pathogens, may facilitate the delivery of immune proteins located on the LD surface. Intracellular LDs can provide infected cells with several biological benefits, serving as a location to attract pathogens as well as coordinating different immune systems that operate simultaneously against different classes of pathogens. LDs may also sequester cytotoxic compounds (such as antimicrobial peptides), reducing damage to other cellular organelles. In view of the widespread resistance to current antibiotics, this study helps decipher molecular mechanisms involved in antimicrobial defense that could be exploited for development of new anti-infective agents. ■

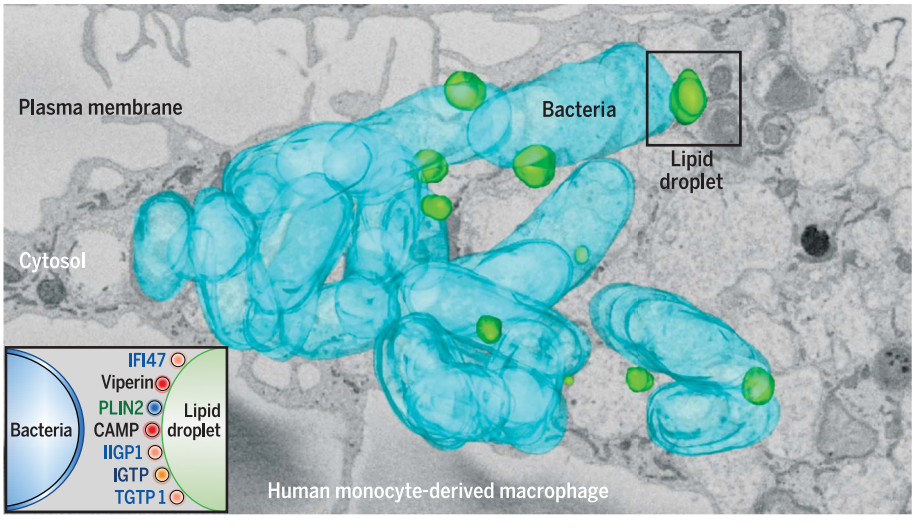

LDs mediate innate immune defense. Serial blockface scanning electron microscopy data reconstruction showing an infected macrophage. Bacteria (blue) and LDs (green) in the three-dimensional dataset have been colored and projected onto a single image. LDs associate with the bacteria surface (black square). This interaction is proposed to bring a specific set of antipathogenic proteins in contact with the membrane-enclosing bacteria (inset).

The list of author affiliations is available in the full article online.
*Corresponding author. Email: martabosch@ub.edu (M.B.); r.parton@imb.uq.edu.au (R.G.P.); apols@ub.edu (A.P.)
†These authors contributed equally to this work.
Cite this article as M. Bosch *et al.*, *Science* **370**, eaay8085 (2020). DOI: 10.1126/science.aay8085

READ THE FULL ARTICLE AT
https://doi.org/10.1126/science.aay8085

RESEARCH ARTICLE

INNATE IMMUNITY

Mammalian lipid droplets are innate immune hubs integrating cell metabolism and host defense

Marta Bosch[1,2]*†, Miguel Sánchez-Álvarez[3]†, Alba Fajardo[1], Ronan Kapetanovic[4,5,6], Bernhard Steiner[4], Filipe Dutra[7], Luciana Moreira[7], Juan Antonio López[8,9], Rocío Campo[8], Montserrat Marí[10,11], Frederic Morales-Paytuví[1], Olivia Tort[1], Albert Gubern[1], Rachel M. Templin[4,12], James E. B. Curson[4,5,6], Nick Martel[4], Cristina Català[13], Francisco Lozano[13], Francesc Tebar[1,2], Carlos Enrich[1,2], Jesús Vázquez[8,9], Miguel A. Del Pozo[3], Matthew J. Sweet[4,5,6], Patricia T. Bozza[7], Steven P. Gross[14], Robert G. Parton[4,12]*, Albert Pol[1,2,15]*

Lipid droplets (LDs) are the major lipid storage organelles of eukaryotic cells and a source of nutrients for intracellular pathogens. We demonstrate that mammalian LDs are endowed with a protein-mediated antimicrobial capacity, which is up-regulated by danger signals. In response to lipopolysaccharide (LPS), multiple host defense proteins, including interferon-inducible guanosine triphosphatases and the antimicrobial cathelicidin, assemble into complex clusters on LDs. LPS additionally promotes the physical and functional uncoupling of LDs from mitochondria, reducing fatty acid metabolism while increasing LD-bacterial contacts. Thus, LDs actively participate in mammalian innate immunity at two levels: They are both cell-autonomous organelles that organize and use immune proteins to kill intracellular pathogens as well as central players in the local and systemic metabolic adaptation to infection.

Lipid droplets (LDs) are the major lipid storage organelles of eukaryotic cells (*1*). Common parasites (such as trypanosomes and *Plasmodium falciparum*), bacteria (such as mycobacteria and *Chlamydia*), and viruses [such as hepatitis C (HCV) and dengue (DENV)] induce and target LDs during their life cycles (*2*). The current view is that LDs support infection, providing invaders with substrates for survival and/or growth (*3*). However, successful innate defense is critical for survival, and host immune responses have coevolved with pathogens, developing a plethora of defense mechanisms. There is some limited evidence that LDs actively participate in innate defense (*4*, *5*). For example, three innate immune system–related proteins localize to the LDs of infected cells: (i) viperin, which is active against two viruses assembled on LDs (HCV and DENV) (*6*); (ii) interferon-γ (IFN-γ)–inducible guanosine triphosphatase (GTPase) (IGTP), which is required for resistance to *Toxoplasma gondii* (*7*); and (iii) histones on LDs, which increase the survival of bacterially challenged *Drosophila* embryos (*8*). We analyzed whether mammalian LDs have a direct or regulated role in immune defense. Because all eukaryotic cells accumulate LDs, this innate defense mechanism may be ubiquitous and therefore serve as a suitable target for therapeutic intervention.

Results

Mammalian LDs display regulated protein-mediated antibacterial activity

We selected hepatic LDs as a proof of concept that mammalian LDs participate in innate immunity. The liver modulates the systemic immune response, and hepatic LDs are targeted by LD-related pathogens (*9*). We tested the antibacterial capacity of hepatic LD proteins in a bacterial killing assay of *Escherichia coli*, an abundant component of the intestinal microbiota and cause of serious clinical infections. First, we injected mice with lipopolysaccharide (LPS), an activator of innate immunity (*10*). Because LPS-treated animals (LPS-mice) reduce food intake, LPS-mice were additionally fasted and compared with mice injected with saline buffer and identically fasted (CTL-mice). Both treatments promoted similar hepatic triglyceride levels (Fig. 1, A, B, and C), although morphological differences between LDs were evident from transmission electron microscopy (TEM). The number of LDs in LPS-treated livers (LPS-LDs) was higher than in those of fasted animals (CTL-LDs), although LPS-LDs were smaller (Fig. 1, D and E). CTL- and LPS-LDs were purified (Fig. 1F and fig. S1A), and LD proteins were incubated with *E. coli*. Bacterial viability was estimated from the resulting colony-forming units (CFUs). LD proteins reduced bacterial growth, and LPS-LD proteins demonstrated enhanced antibacterial capacity (Fig. 1G). This enhancement was confirmed in suspension cultures (fig. S1C) and by use of LD proteins from fed mice (fig. S1, D and E). To determine LD antibacterial activity during an actual infection, mouse liver LDs were obtained after cecal ligation and puncture (CLP), a model of polymicrobial sepsis. CLP-LD proteins exhibited enhanced antibacterial capacity when compared with CTL-LDs (fig. S1, B and F). LPS- and CLP-LD proteins reduced bacterial growth even after a shorter incubation time (fig. S1, G and H). Bacterial growth was unaffected by oleic acid (OA), the major fatty acid component of hepatic LDs, or by cytosolic proteins from CTL- and LPS-livers (fig. S1, I and J). Thus, mammalian LDs have a protein-mediated antibacterial capacity, which is regulated by infection.

Next, we analyzed whether LDs reduce bacterial growth in human monocyte-derived macrophages (HMDMs) from healthy donors. In HMDMs, LD accumulation was promoted by incubation with OA, a fatty acid efficiently esterified into LDs (*11*). Untreated and LD-loaded HMDMs were infected with either nonpathogenic *E. coli* or the professional intramacrophage pathogen *Salmonella enterica* serovar Typhimurium (*Salm*). HMDMs responded to infection by increasing LD numbers (Fig. 1H). *E. coli* survival (Fig. 1I), but not phagocytic capacity (Fig. 1K), was reduced in LD-loaded HMDMs. By contrast, LDs did not reduce *Salm* survival (Fig. 1J), which is in keeping with this pathogen's ability to avoid antimicrobial responses (*12*). In *E. coli*–infected macrophages, LDs were often in the proximity of bacteria (Fig. 1, M to Q). Comparative analyses demonstrated that LDs were closer to and more frequently established longer contacts with *E. coli* than with *Salm* (Fig. 1L and fig. S2, A and B). These LD–*E. coli* contact sites increased in loaded HMDMs (fig. S2, C and D). TEM analysis revealed that in LD–*E. coli* contact sites, the LD monolayer (containing LD proteins) produced an apparent discontinuity in

[1]Cell Compartments and Signaling Group, Institut d'Investigacions Biomèdiques August Pi i Sunyer (IDIBAPS), 08036, Barcelona, Spain. [2]Department of Biomedical Sciences, Faculty of Medicine, Universitat de Barcelona, 08036, Barcelona, Spain. [3]Mechanoadaptation and Caveolae Biology Laboratory, Cell and Developmental Biology Area, Centro Nacional de Investigaciones Cardiovasculares (CNIC). 28029, Madrid, Spain. [4]Institute for Molecular Bioscience (IMB), University of Queensland, Brisbane, Queensland 4072, Australia. [5]IMB Centre for Inflammation and Disease Research, University of Queensland, Brisbane, Queensland 4072, Australia. [6]Australian Infectious Diseases Research Centre, University of Queensland, Brisbane, Queensland 4072, Australia. [7]Laboratório de Imunofarmacologia, Instituto Oswaldo Cruz, FIOCRUZ, Rio de Janeiro, RJ, CEP 21.040-900, Brazil. [8]Cardiovascular Proteomics Laboratory, Vascular Pathophysiology Area, CNIC, Instituto de Salud Carlos III 28029, Madrid, Spain. [9]Centro de Investigación Biomédica en Red, Enfermedades Cardiovasculares (CIBER-CV), Instituto de Salud Carlos III 28029, Madrid, Spain. [10]Department of Cell Death and Proliferation, Institut d'Investigacions Biomèdiques de Barcelona (IIBB)–CSIC, Barcelona, Spain. [11]Hepatocellular Signaling and Cancer Team, IDIBAPS, 08036, Barcelona, Spain. [12]Centre for Microscopy and Microanalysis, University of Queensland, Brisbane, Queensland 4072, Australia. [13]Immunoreceptors of the Innate and Adaptive System Team, IDIBAPS, 08036, Barcelona, Spain. [14]Department of Developmental and Cell Biology, University of California, Irvine, Irvine, CA 92697, USA. [15]Institució Catalana de Recerca i Estudis Avançats (ICREA), 08010, Barcelona.
*Corresponding author. Email: martabosch@ub.edu (M.B.); r.parton@imb.uq.edu.au (R.G.P.); apols@ub.edu (A.P.) †These authors contributed equally to this work.

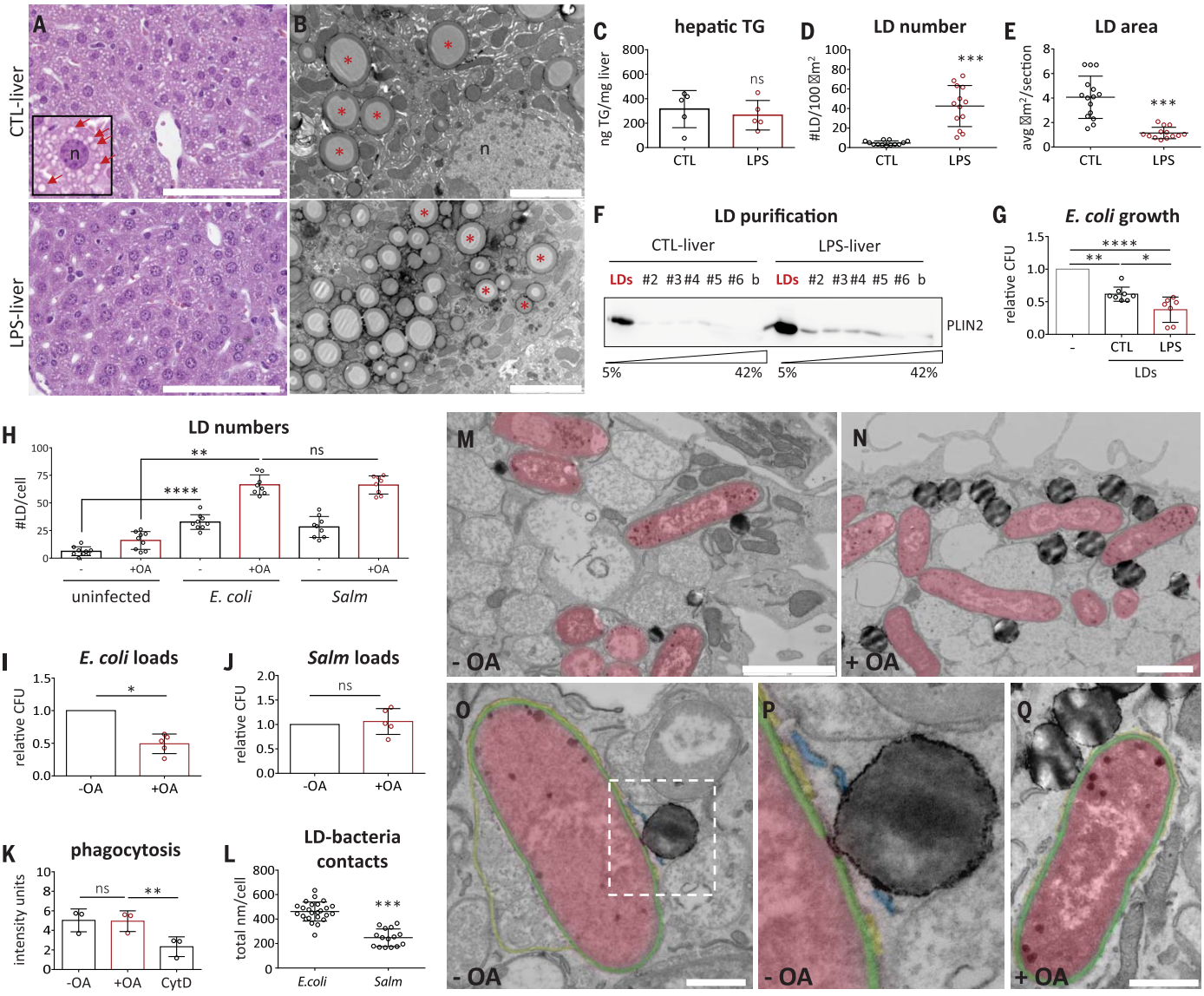

Fig. 1. Mammalian LDs display regulated protein-mediated antibacterial activity. (**A**) H&E-stained sections and (**B**) TEM images of (top) CTL- or (bottom) LPS-livers. Red arrows [(A), inset] and asterisks (B) indicate LDs, and "n" indicates the selected hepatocyte nucleus. Images are representative of (A) five or (B) two mice per condition. Scale bars, 100 µm (A) and 5 µm (B). (**C**) Hepatic triacylglycerol levels (TG) in CTL- and LPS-mice (five mice per condition). (**D**) Hepatic LD number and (**E**) mean LD area measured in TEM images of CTL- or LPS-livers. For each condition, at least 13 random liver sections, obtained from two mice per condition, were quantified (fig. S6). (**F**) CTL- and LPS-livers were fractionated in sucrose density gradients, and LDs floated onto the top fraction ("LDs"), as assessed with anti-PLIN2 immunoblotting (fig. S1A) (representative of five mice per condition). (**G**) *E. coli* were incubated for 16 hours in (gray) standard medium or medium supplemented with proteins from (black) CTL- or (red bar) LPS-LDs. CFU measurements were normalized to the standard medium condition ($n \geq 7$ independent experiments) (fig. S1). (**H**) Unloaded (black) and OA-loaded HMDMs (red bars) were infected with *E. coli* or *Salm* for 4 hours. LD number per cell was quantified in TEM images. At least eight macrophages per group, obtained in three independent experiments, were analyzed. (**I** and **J**) Control (black) and OA-loaded HMDMs (red bars) were infected with (I) *E. coli* or (J) *Salm* and bacterial loads (CFU) determined 24 hours later ($n = 5$ independent experiments). (**K**) Control (black) and OA-loaded HMDMs (red bars) were incubated with pHrodo *E. coli* and bacterial loads measured (fluorescence units) ($n = 3$ independent experiments). Cyt D was used to inhibit phagocytosis. (**L**) Length of LD-bacteria contacts per cell was measured in TEM images of OA-loaded HMDMs infected with *E. coli* or *Salm* for 4 hours. At least 15 macrophages per group, obtained in three independent experiments, were analyzed (fig. S2, A to D). (**M**, **O**, and **P**) Control and (**N** and **Q**) OA-loaded HMDMs were infected with *E. coli* for 4 hours and analyzed in TEM images. Representative images have been pseudocolored blue (ER), red (*E. coli* interior), green (periplasm), and yellow (vacuolar membrane) (fig. S2, E and F) (representative of three independent experiments). Scale bars, 2 µm [(M) and (N)] and 0.5 µm [(O) and (Q)]. All graphs show means ± SD; ns, not significant; $*P < 0.05$, $**P < 0.01$, $***P < 0.001$, $****P < 0.0001$ in a paired *t* test [(C) to (E), (H) to (J), and (L)], and one-way ANOVA test [(G) and (K)].

the bacterial vacuolar membrane and probably interacted with the bacterial periplasm (Fig. 1, O to Q, and fig. S2, E and F). Thus, LD-loaded macrophages display enhanced antibacterial capacity, which suggests the existence of docking mechanisms that enable or facilitate the engagement of antibacterial LD proteins with bacteria.

Quantitative mass spectrometry analysis of LPS-LDs

To characterize the enhanced LPS-LD antibacterial capacity, we performed comparative mass spectrometry profiling of proteins differentially associated with LPS- or CTL-LDs (*13*). CTL- and LPS-livers were analyzed in parallel. Stringent analysis [false discovery rate (FDR) < 1] of LPS-livers identified 8563 proteins, of which 1136 (cut-off $|\Delta Zq| \geq 1.8$, where ΔZq reflects the differential Zq score for a protein in LPS-livers when compared with CTL-livers.) were differentially expressed (553 enriched and 583 reduced) (Fig. 2A and tables S1 and S2). In LPS-LDs, 3392 proteins were identified (table S3), of which 689 were differentially distributed (317 enriched and 372 reduced) (tables S4 and S5). Only 8% of the enriched and 0.8% of the down-regulated proteins in LPS-LDs followed an equivalent profile in LPS-livers (Fig. 2, A and B, and fig. S3A), indicating autonomous changes in LPS-LDs. Functional annotation enrichment analysis revealed the up-regulation of proteins related to the acute phase and inflammatory responses and reduction of mitochondrial proteins cofractionating with LDs (Fig. 2B and fig. S2A).

Published proteomic analyses show that ~7 to 10% of proteins in LD fractions are bona fide LD-resident proteins (*14*, *15*), reflecting the tight interaction of LDs with other organelles. Of 3392 identified proteins in LPS-LDs, 238 (7%) were annotated as LD-resident proteins with the Ingenuity Pathway Analysis (IPA) platform or with at least one of the above proteomic analyses (Fig. 2C and table S6). Of these LD proteins, 72 were LPS-regulated (59 enriched and 13 reduced) (table S7). Thus, 30% of the identified LD proteome, including the five perilipins (PLINs), was LPS-sensitive. PLIN2 (ΔZq = 6.47) and RAB18 (ΔZq = 7.10) were highly enriched, and PLIN5 was the only down-regulated PLIN (ΔZq = −4.13) (table S7). Two immune proteins previously described on LDs, viperin (RSAD2, ΔZq = 8.12) and IGTP (IRGM3, ΔZq = 6.7), were identified on LPS-LDs, validating our proteomic strategy (table S4). IPA analysis of these LD-resident proteins demonstrated enrichment of innate immunity–related components and reduction of metabolism-related LD-resident proteins (fig. S3B).

To identify relevant candidates on LPS-LDs, we initially performed hierarchical clustering of proteins with similar variation profiles across each individual replicate, likely reflecting coregulation (Fig. 2D). Gene interaction analysis of correlated proteins revealed the existence of several functionally connected protein networks, such as clusters of RAB GTPases, a cluster containing PLIN1 and histones, and a network of metabolism regulators, including PLIN3, PNPLA2 (ATGL), and ACSL4 (fig. S4A). The cluster containing proteins ranking highest for enrichment (ΔZq > 3.14) nucleated around PLIN2 and included viperin, IGTP, and several immune GTPases (GVIN, IFGGA1, IFGGB55, IFI47, and IFI35) (Fig. 2D). These functionally related proteins may also physically interact. We confirmed that PLIN2 interacts with IGTP (*7*) and detected a weak interaction with cathelicidin (fig. S4B). Last, we performed a gene interaction analysis across the whole LPS-sensitive LD proteome (ΔZq > 1.8). This analysis retrieved complex protein networks (Fig. 2E), suggesting that LDs are innate immune hubs integrating major intra- and extracellular responses.

We validated the proteomic data with immunoblotting and confirmed enrichment of PLIN2 and PLIN3 on LPS-LDs in contrast with the unregulated lipase HSL (ΔZq = 0.04) (Fig. 3A). PLIN2 expression was further confirmed in mouse liver sections (fig. S5A). PLIN2 in LPS- and CLP-livers was predominantly expressed in hepatocytes around periportal regions where cells receive blood and regulatory inflammatory mediators. Direct transcriptional regulation of LD proteins by inflammatory stimuli (fig. S5B) was assessed in human hepatic HuH7 cells treated with LPS, tumor necrosis factor (TNF), or IFN-γ. *PLIN2* and *PLIN5* expression was differentially regulated by individual cytokines (fig. S5C). Thus, LPS likely regulates LD protein composition directly and in conjunction with paracrine signaling networks.

Physical and functional uncoupling of LPS-LDs and mitochondria

Mitochondria are key organelles for innate immunity (*16*). During nutrient starvation, LDs contact mitochondria to supply fatty acids, fueling oxidative phosphorylation (OXPHOS) (*17*). By contrast, challenged innate immune cells increase aerobic glycolysis and reduce OXPHOS (*16*). Therefore, uncoupling LPS-LDs and mitochondria (Fig. 2B) may contribute to a reduction of OXPHOS in infected cells. Reduced interaction between LPS-LDs and mitochondria was confirmed through decreased cofractionation of ATP5D [a subunit of adenosine 5′-triphosphate (ATP) synthase, an OXPHOS enzyme] when compared with CTL-LDs (Fig. 3, A and B). Functional annotation of reduced mitochondrial proteins cofractionating with LPS-LDs matched with the whole mitochondrial proteome (MitoCarta 2.0) (Fig. 3C). This does not reflect a reduced mitochondrial content of LPS-livers as determined by hepatic citrate synthase activity and liver cytochrome oxidase (*COI*) gene copy number (Fig. 3, D and E). The reduced number of contacts between LPS-LDs and mitochondria was then confirmed with TEM (Fig. 3F and fig. S6). In these images, endoplasmic reticulum (ER) membranes often separated LPS-LDs and mitochondria (fig. S6C). Last, we confirmed two functional consequences of uncoupling: (i) reduced mitochondrial β-oxidation of lipids supplied by LDs in LPS-primary hepatocytes (Fig. 3, G and H) and (ii) lower levels of circulating ketones in LPS-mice serum (Fig. 3I). These results extend and mechanistically explain early observations showing reduced β-oxidation and ketogenesis in rats infected with *Streptococcus pneumoniae*, *Francisella tularensis*, and *S.* Typhimurium (*18*).

PLIN5 tethers LDs and mitochondria (*17*). PLIN5 is the only PLIN down-regulated in LPS-LDs (fig. S3B and tables S5 and S7). During fasting, to facilitate LD-mitochondria contacts, PLIN5 levels increase on hepatic LDs (Fig. 3J). However, PLIN5 levels on LDs were reduced when fasted mice were treated with LPS (Fig. 3, A and J). Further, human *PLIN5* expression promoted coclustering of LDs and mitochondria in HuH7 cells (Fig. 3K). To explore the role of PLIN5 during infection, *PLIN5* was transfected in LPS-responsive human embryonic kidney (HEK) 293-TLR4$^+$ cells (fig. S7, A to C), and the LD-mitochondria contacts were quantified. *PLIN5* expression increased the number and length of these contacts (Fig. 3L and fig. S7, D to F). In LPS-treated HEK293-TLR4$^+$ cells, the overall length of the contacts was reduced in CTL- but not in *PLIN5*-expressing cells (Fig. 3L). In *PLIN5*-expressing cells, LPS only modestly reduced the total number of contacts (fig. S7E) and increased the average length of remaining contacts (fig. S7F). Thus, LPS directly regulates dynamics of LD-mitochondria contacts. Furthermore, PLIN5 down-regulation appears to be involved in the LPS-induced metabolic reprogramming.

We next evaluated the role of PLIN5 in other aspects of immune defense. *PLIN5*-overexpressing HEK293 cells exhibited a significantly reduced capacity to clear *E. coli* by comparison with that of *PLIN3*-overexpressing control cells (Fig. 3, M and N). Furthermore, THP-1 cells lentivirally transduced with *PLIN5* and subsequently infected with *E. coli* exhibited increased numbers of LD-mitochondria contacts (fig. S7, G to I), reduced LD-bacteria interactions (fig. S7J), and impaired antimicrobial capacity (Fig. 3, O and P). Thus, LPS-mediated PLIN5 down-regulation reduces LD-mitochondria tethering, enabling an effective antimicrobial response.

LDs accumulate and use innate immune proteins

Our proteomic analyses predicted complex immune protein networks on LDs (Fig. 2, D and E,

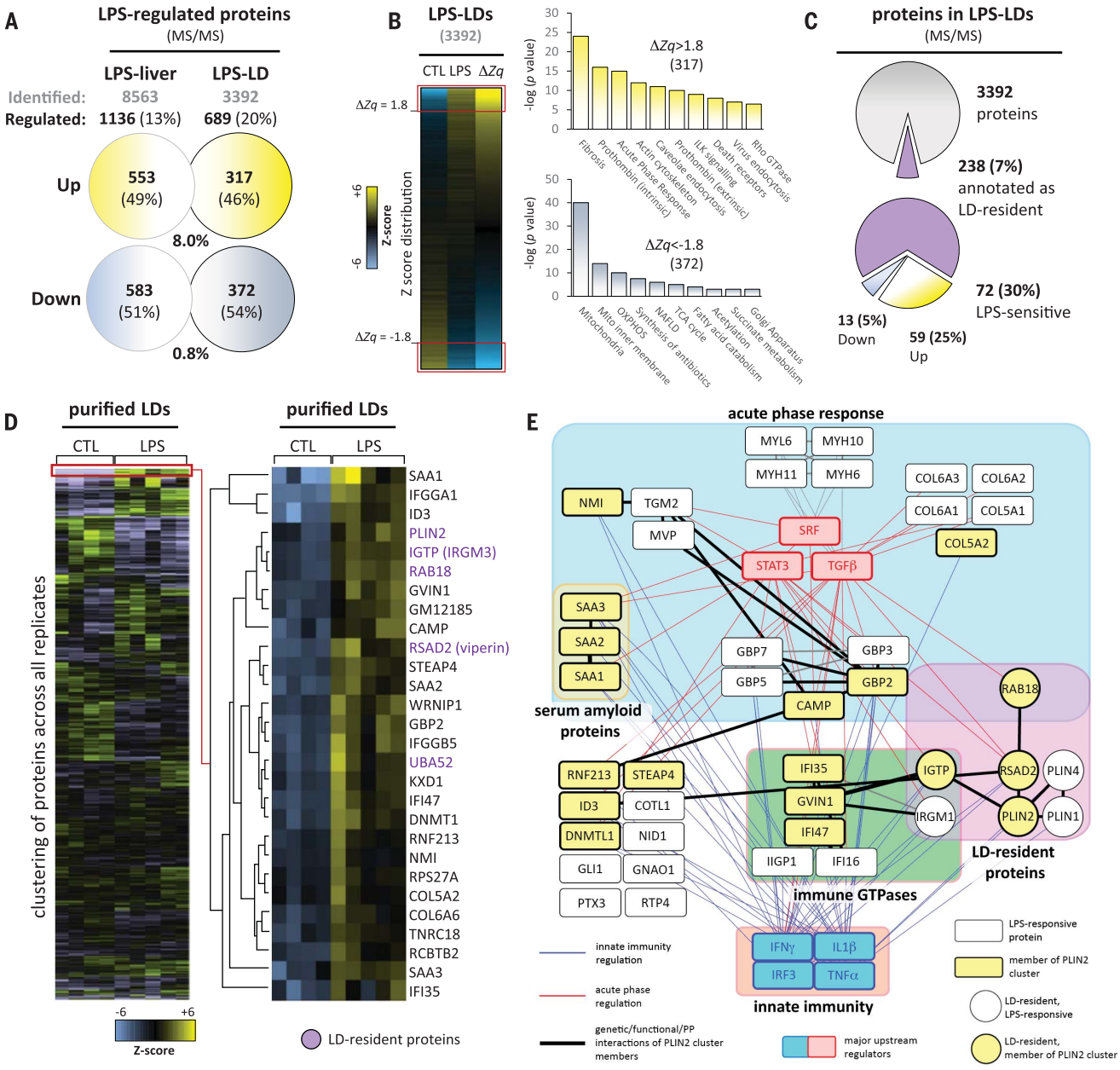

Fig. 2. Quantitative mass spectrometry analysis of LPS-LDs. (**A**) Summary of changes in the proteome of LPS-livers (n = 3 independent mice) and LPS-LDs (n = 5 independent LD fractions) when compared with those in CTL-livers (n = 3 independent mice) or CTL-LDs (n = 4 independent LD fractions), respectively. "Identified" (gray letters) indicates identified proteins, and "Regulated" (black letters) indicates proteins significantly cut-off $|\Delta Zq| \geq 1.8$ modified by LPS. Among modified proteins, yellow and blue circles indicate up- and down-regulated proteins, respectively (tables S1 to S5). (**B**) Functional annotation enrichment analysis of proteins increasing ($|\Delta Zq| > 1.8$; yellow graphs) or decreasing ($|\Delta Zq| < -1.8$; blue graphs) on LPS-LDs when compared with CTL-LDs. Enrichment as compared with the mouse genome for each category is expressed as −log (P value). Analyses for CTL- and LPS-livers are shown in fig. S3A. (**C**) Pie charts summarizing LPS-induced changes in bona fide LD proteins. Protein details are in tables S6 and S7, and annotated interactions are provided in fig. S3B. (**D**) Hierarchical clustering of Zq values across replicates identifies functionally coherent protein subsets similarly regulated by LPS [threshold for cluster analysis, correlation coefficient (r) > 0.78]. The cluster nucleated around PLIN2 is included. Five additional clusters are detailed in fig. S4A. (**E**) Gene subnetwork from IPA analysis of all identified proteins up-regulated in LPS-LDs.

and fig. S4A). Given that many known antipathogenic proteins were associated with the PLIN2 cluster (Fig. 2D), we next assessed components of this cluster for LD association. The antiparasitic protein IGTP and the antiviral protein viperin as well as three GTPases (IIGP1, TGTP1, and IFI47) all associated with LDs (Fig. 4, A to C, and figs. S8 and S9). Thus, multiple proteins associated with responses to different classes of pathogens localize to LDs.

The PLIN2 cluster also includes cathelicidin (CAMP; ΔZq = 7.25), a broad-spectrum antimicrobial peptide with chemotactic and immunomodulatory properties (*19*). Cathelicidins are synthesized as proproteins which, after cleaving an N-terminal signal peptide, follow the exocytic pathway (fig. S10A). We confirmed the accumulation of CAMP on LPS-LDs (Fig. 4A) and the distribution of a human-tagged CAMP between the ER and LDs of HuH7 cells (Fig. 4B and fig. S10, B to E). CAMP on LDs had a

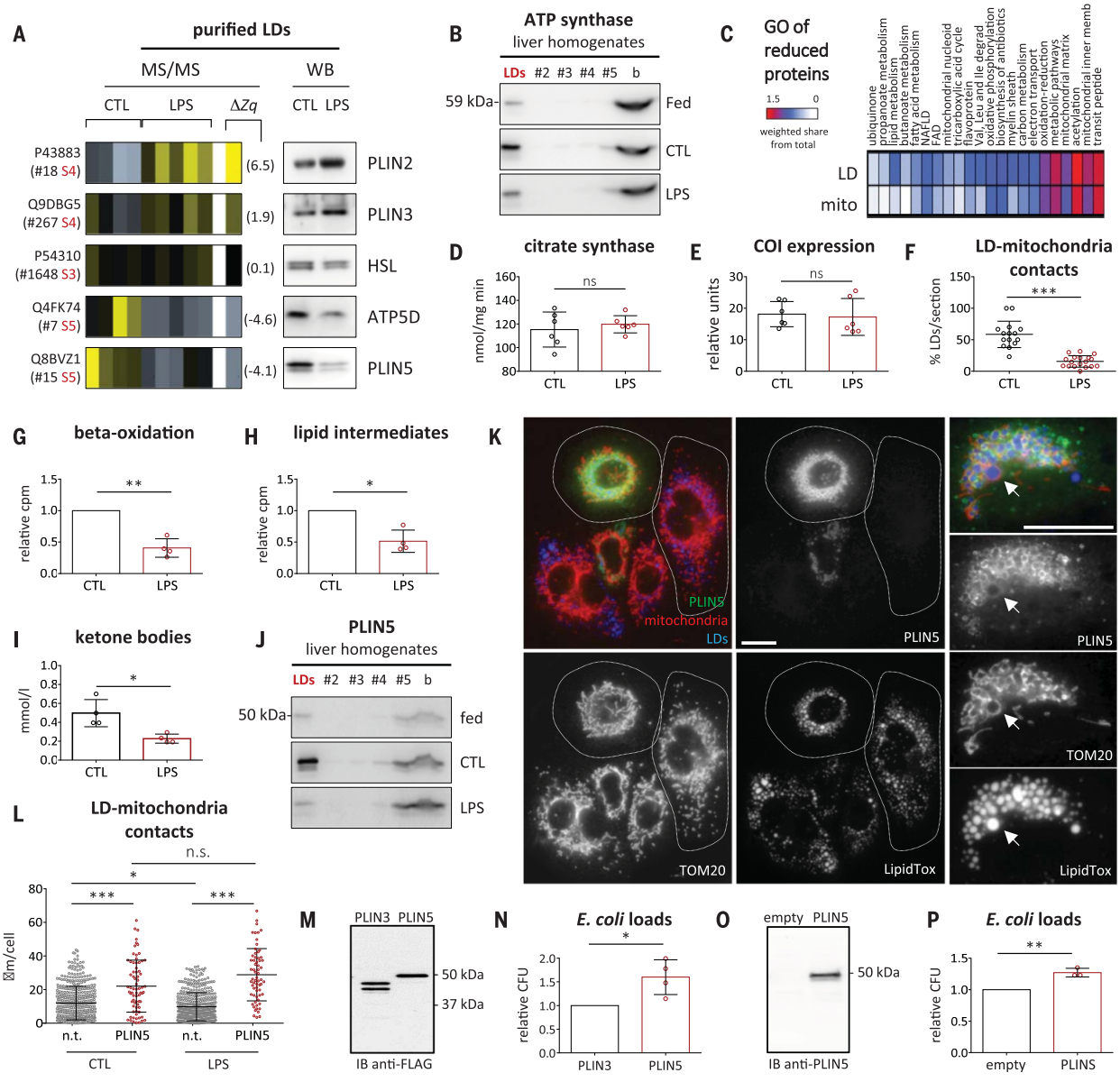

Fig. 3. Physical and functional uncoupling of LPS-LDs and mitochondria.
(**A**) Relative enrichment of selected proteins. Protein enrichment in LPS-LDs illustrated by a heatmap code (blue, depletion; yellow, enrichment). The Δ*Zq*, UniProt ID, ranking (tables S3 to S5), and a representative immunoblot (representative of three mice per condition) are indicated. (**B**) Fed-, CTL-, and LPS-livers were fractionated in sucrose gradients, and LD–mitochondria cofractionation was determined through immunoblotting of ATP5D (a subunit of ATP synthase) (representative of three mice per condition). (**C**) Functional categories of down-regulated mitochondrial proteins cofractionating with LPS-LDs are compared with the whole mitochondrial proteome (MitoCarta 2.0). (**D** and **E**) The mitochondrial content of CTL- (black) and LPS-livers (red bars) was determined from (D) citrate synthase activity and (E) DNA copy number of COI (relative to GAPDH) (n = 6 independent livers). (**F**) Percentage of LDs interacting with mitochondria in CTL- (black) and LPS-livers (red bars) was quantified in TEM images. At least 15 random sections, obtained from two mice per condition, were analyzed (fig. S6). (**G**) Mitochondrial beta-oxidation and (**H**) formation of soluble intermediates (ketone bodies) of lipids stored in LDs were quantified for 16 hours in primary hepatocytes left untreated (black) or treated with LPS (red bars) (four mice per condition). (**I**) Ketones in sera of CTL- (black) and LPS-mice (red bars) (four mice per condition). (**J**) Fed-, CTL-, and LPS-livers were fractionated in density gradients and PLIN5 distribution analyzed by immunoblotting (representative of five mice per condition). (**K**) HuH7 cells were transfected with a tagged *PLIN5* and labeled with anti-FLAG antibodies (PLIN5), anti-TOM20 antibodies (mitochondria), and LipidTox (LDs). Contours of a representative transfected and nontransfected cell are indicated. (Right) An additional transfected cell. The arrows indicate a mitochondrion completely enwrapping a LD (representative of three independent experiments). Scale bar, 20 μm. (**L**) LPS-sensitive HEK293-TLR4$^+$ cells transfected with a tagged *PLIN5* were loaded with OA (black) or with OA+LPS (red dots). The length of LD-mitochondria contacts per cell was measured in confocal microscopy images (an example is available in fig. S7, D to F). Sixty-six transfected cells and 470 nontransfected cells, obtained from three independent experiments, were analyzed. (**M** and **N**) HEK293 cells were transfected with FLAG-tagged *PLIN3* or *PLIN5* and loaded with OA, and (M) protein expression was determined by means of immunoblotting. (N) Cells were infected with *E. coli*, and bacterial loads quantified after 4 hours (n = 4 independent experiments). (**O** and **P**) THP-1 cells were transduced with *PLIN5*-encoding or empty lentiviral vectors. (O) PLIN5 expression was confirmed through immunoblotting. (P) Transduced cells were infected with *E. coli*, and bacterial loads were evaluated after 8 hours (n = 3 independent experiments) (fig. S7, G to J). All graphs show means ± SD; ns, not significant; $^*P < 0.05$, $^{**}P < 0.01$, $^{***}P < 0.001$, in a paired t test [(D), (E), (G) to (I), (M), and (N)], one-way ANOVA test (L), and two-sided Student's z test on proportions (F).

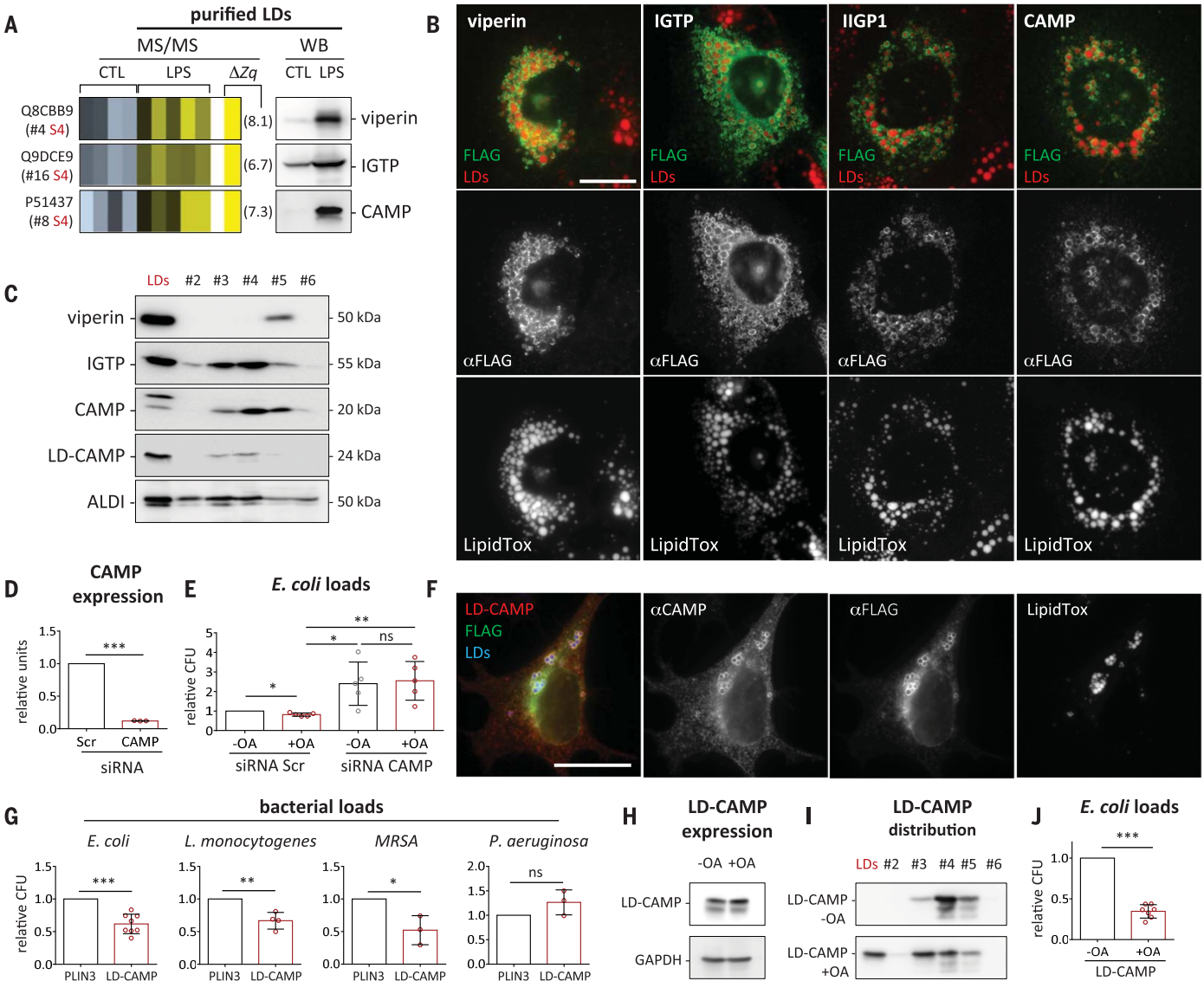

Fig. 4. LDs accumulate and use innate immune proteins. (**A** to **C**) Relative enrichment of selected proteins. Protein enrichment in LPS-LDs was evaluated as in Fig. 3. Accumulation of transfected proteins on LDs was confirmed in HuH7 cells by means of (B) immunofluorescence and (C) fractionation in density gradients (figs. S8 to S10 and S12). Scale bar, 20 μm. (**D** and **E**) HMDMs were transfected with a scrambled (Scr) or with a CAMP siRNA, and (D) CAMP expression was determined by means of quantitative RT-PCR. Then, unloaded and OA-loaded HMDMs were infected with *E. coli* for 8 hours, and bacterial loads (CFU) were quantified (n = 5 independent experiments). (**F**) HEK293 cells were transfected with a tagged LD-*CAMP* (fig. S12) and loaded with OA. LD-CAMP was detected on LDs (LipidTox) with antibodies to FLAG and to CAMP. The image is representative of three independent experiments. Scale bar, 20 μm. (**G**) HEK293 cells were transfected with LD-*CAMP* (red) or *PLIN3* (black bars), loaded with OA, and infected with the indicated bacteria for 4 hours. Bacterial loads were quantified, and CFU values were normalized to *PLIN3*-cells ($n \geq 3$ independent experiments). (**H** to **J**) LD-*CAMP*–transfected HEK293 cells were incubated in control (black) or OA containing medium (red). (H) Cellular LD-CAMP levels and (I) LD accumulation were assessed through immunoblotting with anti-CAMP antibodies. (J) These cells were then infected with *E. coli* for 4 hours, and bacterial loads were quantified (n = 7). All graphs show means ± SD; ns, not significant; $^{*}P < 0.05$, $^{**}P < 0.01$, $^{***}P < 0.001$ in a paired t test.

higher molecular weight than that of CAMP in the ER (Fig. 4C and fig. S10E), suggesting that the CAMP hydrophobic domain functions as both a signal peptide cleaved for secretion via the ER as well as an uncleaved LD-targeting signal. An equivalent dual distribution occurs for other LD proteins that contain signal peptides, such as apolipoproteins (*20*). The low–molecular weight (20 kDa) CAMP species corresponded to the protein with a cleaved signal peptide following the secretory pathway (fig. S10, F to H). Distribution of overexpressed CAMP, as well as other immune LD proteins, was not directly affected by LPS-TLR4 signaling (fig. S11). Thus, LPS does not directly regulate the intracellular trafficking of these proteins.

We next investigated the role of CAMP in HMDMs. Silencing of *CAMP* (Fig. 4D) impaired the antibacterial response of the macrophages against *E. coli* (Fig. 4E). Furthermore, although LD loading significantly reduced bacterial survival, this treatment regime was unable to do so in CAMP-silenced HMDMs. Thus, the antibacterial activity of LDs in HMDMs appears to require CAMP. To further explore this possibility, a LD-resident CAMP was engineered through substitution of the CAMP signal peptide with

the ALDI LD-targeting motif (fig. S12, A and B) (*21*). Modified CAMP (LD-CAMP) accumulated on LDs of HuH7 cells (fig. S12, C to F) and showed a single electrophoretic mobility pattern, matching the higher–molecular weight CAMP that localized to LDs (Fig. 4C and fig. S12C). Next, HEK293 cells were transfected with LD-*CAMP*, and protein distribution on LDs was confirmed with antibodies to CAMP (Fig. 4F), demonstrating a native conformation. The antimicrobial capacity of LD-CAMP was then assessed. Bacterial loads of *E. coli*, *Listeria monocytogenes*, and methicillin-resistant *Staphylococcus aureus* (MRSA) were significantly reduced in LD-*CAMP*–expressing cells when compared with those expressing the *PLIN3* control (Fig. 4G). By contrast, *Pseudomonas aeruginosa* loads were not affected by LD-*CAMP*, suggesting that this pathogen subverts this innate defense response. The impact of LD-*CAMP* overexpression on bacterial survival was dependent on LD formation (Fig. 4, H to J). The tagged LD-*CAMP* demonstrated a similar antibacterial activity to that of wild-type *CAMP* and a slightly augmented stability when compared with an untagged LD-*CAMP* (fig. S12, G to J). Thus, LDs act as a molecular switch in innate immunity, responding to danger signals by both reprogramming cell metabolism and eliciting protein-mediated antimicrobial defense.

Discussion

Pathogens require host-derived lipids to support their life cycles, with LDs providing a source of these lipids (*22*). As a result, LDs also have the potential to deliver effective host defenses against intracellular pathogens. We show that at least 30% of the LD proteome is LPS-sensitive, suggesting that innate immunity has developed a host defense program that includes extensive LD remodeling. Our analyses demonstrate that complex clusters of immunity-related proteins organize on LDs of infected cells. In addition to previously described LD-resident immune proteins, such as viperin and IGTP, we have identified IIGP1, TGTP1, and IFI47. Our analysis also identified CAMP as a professional antibacterial protein efficiently functioning on LDs. These proteins may act individually, in a coordinated manner, and/or synergistically to kill pathogens.

Mechanisms of LD trafficking and docking with phagocytic and parasitophorous membranes, observed here and described for several pathogens (*23*–*26*), may facilitate the delivery of immune proteins located on the LD surface. Accumulation on LDs may provide stability to these proteins and may restrict these potentially cytotoxic peptides to LDs, preventing indiscriminate cellular damage (*27*). In this respect, we have shown that LPS triggers physical separation of LDs and mitochondria, at least partly because of reduced PLIN5 levels on LPS-LDs (*28*). Uncoupling likely reflects both a self-protection program (to avoid mitochondrial damage, in view of their prokaryotic evolutionary origin) and a means to maximize or increase the number of LDs available to interact with bacteria. Simultaneously, the reduced LD-mitochondria interaction may lead to distinctive immunometabolic features: (i) the accumulation of host LDs, resulting from reduced mitochondria-mediated LD consumption; (ii) reduced OXPHOS displayed by infected cells, owing to decreased fatty acid oxidation; and (iii) the low rates of ketogenesis displayed by infected animals.

These studies highlight that mammalian LDs constitute an intracellular first line of defense. LDs actively participate in at least two levels of the innate immune response, accumulating and using antibacterial proteins as well as regulating immune cell metabolism. Because widespread resistance to current antibiotics is common among pathogens, understanding the cellular mechanisms that elicit LD-mediated defense may inform future strategies for the development of anti-infective therapies (*29*, *30*).

Materials and methods

Plasmids

pCMV6-*IGTP*-myc-FLAG (MR224617), pCMV6-*CAMP*-myc-FLAG (RC208872), pCMV6-*IIGP1*-myc-FLAG (MR206520), pCMV6-*TGTP1*-myc-FLAG (MR206553), and pCMV6-*IFI47*-myc-FLAG (MR206684) were purchased from OriGene Technologies (Rockville, Maryland). pcDNA3.1-*VIPERIN*-FLAG (OHu13432) was from Genscript (Piscataway, New Jersey). pcDNA3.1- *PLIN5*-FLAG (OHu04126) from GenScript was subcloned into pCMV6-myc-FLAG vector using primers containing EcoRI and XmaI sites. The LD-*CAMP* construct was derived from the plasmid pCMV6-*CAMP*-myc-FLAG: an equivalent EcoRI/BspEI sequence of pCMV6-*CAMP*-myc-FLAG was designed replacing the *CAMP* signal peptide (MKTQRDGHSLGRWSLVLLLLGLVMPLAII) with the hydrophobic domain of *ALDI* (MDALVLFLQLLVLLLTLPLHLLALLGC) acquired from GeneScript, cloned in a PUC57 plasmid. Both fragments were swapped after an EcoRI/BspEI digestion. *CAMP* ΔN mutant, results from deletion of the amino acids 1-32. The cDNAs were acquired from GenScript and subcloned into pCMV6-myc-FLAG vector following the same strategy. pCMV6-*CAMP*-untagged was generated by polymerase chain reaction (PCR) using primers containing EcoRI and XmaI sites. The plasmid pCMV6-*PLIN2*-myc-FLAG tagged was derived from the plasmid pGFP-*PLIN2*, provided by Dr John McLauchlan (Institute of Virology, Glasgow) and subcloned into pCMV6 by PCR using primers containing EcoRI and XhoI sites. The plasmid pCMV6- *PLIN3*-myc-FLAG tagged was derived from the plasmid pCDNA 3×myc-tagged *PLIN3* provided by S. Pfeffer (Stanford University School of Medicine, Stanford, California), and subcloned into pCMV6 by PCR using primers containing EcoRI and XhoI sites. The lentiviral system utilizing pFTRE3G-PGK-puro (kindly provided by James Murphy, Walter and Elizabeth Hall Institute of Medical Research) for doxycycline-inducible gene expression has previously been described (*31*, *32*). The plasmid pFTRE3G-*PLIN5* was obtained by subcloning *PLIN5* into pFTRE3G by PCR using primers containing BamHI sites.

Mouse studies

Animals and models of infection

C57BL/6J male mice (8 to 10 weeks old) were purchased from Charles River Laboratories (Wilmington, Massachussetts). Animals were kept under a controlled humidity and lighting schedule with a 12 hours dark period. Food and water were available ad libitum. All animals received humane care in compliance with institutional guidelines regulated by the European Community. The experimental protocols were approved by the Animal Care Committee of the University of Barcelona. The day before the experiment, animals were fasted overnight (16 hours) and in some cases intraperitoneally injected with 200 μl of saline buffer (CTL) or 6 mg/kg LPS (final dose) (L2639, Sigma-Aldrich, St Louis, Missouri). In some experiments (fed condition) food was available ad libitum. To induce sepsis by cecal ligation and puncture (CLP), mice were anesthetized with an intraperitoneal injection of 100 mg/kg ketamine (Richter Pharma AG, Wels) and 10 mg/kg xylazine (Rompun, Bayer, Leverkusen, Germany) and a 1-cm incision was made on the abdomen. The cecum was exposed and ligated below the ileocecal junction. A double puncture was made using a 22G needle, to induce severe sepsis. Sham-operated animals (CTL) underwent an identical laparotomy but without CLP. All mice received 1 ml of sterile saline subcutaneously as fluid resuscitation and antibiotic therapy by subcutaneous injection of 10 mg/kg meropenen (Merck Research Laboratory, Whitehouse Station, New Jersey) 6 hours after surgery.

Histological analysis

Liver sections were prepared and processed for hematoxylin and eosin (H&E) staining as previously described (*33*). For immunohistochemistry, liver sections were prepared and processed as described previously (*34*). The slides were blocked by incubation in 5% normal goat serum in PBS for 1 hour at room temperature followed by incubation with anti-PLIN2 antibody (1:200; ab78920, Abcam, Cambridge, UK) overnight at 4°C. Sections were then washed three times in PBS and incubated with secondary goat anti-rabbit immunoglobulin G (IgG) Alexa Fluor 647 (1:250; A21244, ThermoFisher Scientific, Waltham, Massachussetts)

for 45 min at RT. After washing three times in PBS, slides were mounted with Dako Fluorescence Mounting Medium (Agilent Dako, #S3023).

Liver fractionation and hepatic LD purification

After liver perfusion with 0.9% NaCl and 0.1% EDTA solution, the liver was placed on a Petri dish, chopped with a scalpel for two min and transferred into a Dounce tissue grinder at a ratio of 1 g of tissue to 3 ml of homogenization buffer (25 mM Tris-HCl, pH 7.5, 100 mM KCl, 1 mM EDTA, and 5 mM EGTA). After three up-and-down strokes of each loose- and tight-pestle, the liver homogenate was centrifuged at 500*g* for 10 min at 4°C. 2.5 ml of the resulting post-nuclei supernatant (PNS) were mixed with an equal volume of 2.5 M sucrose and placed at the bottom of a sucrose step gradient of 25%, 15%, 10%, and 5% (w/v) sucrose in homogenization buffer, with an additional top layer of 25 mM Tris-HCl, pH 7.5, 1 mM EDTA and 5 mM EGTA, and centrifuged at 12,000*g* for 1 hour at 4°C (SW-41Ti rotor, Beckman Coulter, Pasadena, California). Six or seven fractions were collected from the top. Equal volumes of each fraction were used for immunoblotting. To purify LDs, the LD fraction on the top of the gradient was recovered and concentrated by re-floating LDs at 16,000*g* for 10 min at 4°C. The lower phase containing the excess buffer was removed by aspiration with a syringe and four volumes of ice-cold acetone were added to precipitate proteins and kept 48 hours at -20°C. The samples were centrifuged at 16,000*g* for 10 min at 4°C, the pellet washed with cold acetone 3 times, air-dried and reconstituted with 10 mM Tris-HCl, pH 7.5. After sonication, protein concentration was quantified by CBQCA protein quantitation kit (ThermoFisher Scientific). To purify cytosol extracts, 200 µl of PNS plus 600 µl of homogenization buffer were centrifuged at maximal speed for 1 hour ($1 \times 10^6 g$ in S140-AT Fixed Angle Rotor, ThermoFisher Scientific). A syringe (23G needle) was inserted below the floating LDs to remove 200 µl of cytoplasm and proteins were precipitated as described previously.

Bacterial killing assay (BKA)

E. coli (ATCC 25922) were grown to an O.D. at 600 nm of 1 and diluted 1:100 (1.5×10^5 colony-forming units (CFU/ml)). One hundred microliters of bacterial culture were mixed with 15 or 25 µg of LD-proteins. Incubation buffer (33 mM KH_2PO_4, 60 mM K_2HPO_4, 10 mM Na_2SO_4, 1.7 mM sodium citrate, 10 mM $MgSO_4$) was then added up to 200 µl. Cultures were incubated for the indicated times at 37°C in a shaking incubator. Serial dilutions were plated in triplicate on LB-agar plates and surviving bacteria were quantitated as CFU/ml after overnight incubation at 37°C. Alternatively, overnight incubations were centrifuged at 11,000*g* for 30 s and the bacterial pellet was resuspended in PBS and measured the absorbance by optical density at 600 nm with a Modulus Microplate Multimode Reader (Promega, Madison, Wisconsin). For monitoring bacterial growth in the presence or absence of OA (175 µg/ml) or gentamicin (200 µg/ml), *E. coli* cultures were diluted to an O.D. at 600 nm of 0.1 in 96-well flat-bottom plates and incubated at 37°C shaking. O.D. at 600 nm readings were taken every 20 min and monitored using a POLARstar Omega reader (BMG Labtech, Germany).

Serum parameters, hepatic triacylglycerol quantification, and mitochondrial content

Blood was extracted by cardiac puncture and sera obtained after centrifugation of blood samples at 6,000*g* for 15 min at 4°C in serum heparin separator tubes (Becton Dickinson, Franklin Lakes, New Jersey). Ketone bodies in serum were measured using a Ketone Body Assay Kit (MAK134; Sigma-Aldrich) according to the manufacturer's instructions. Triacylglycerol content of the liver was determined using the Triglyceride Detection Kit following manufacturer's instructions (BioSystems, Barcelona, Spain). Citrate synthase activity was measured as a reliable marker of mitochondrial content as previously described (*35*).

Fatty acid beta-oxidation

Primary hepatocytes were isolated as previously (*36*). To accumulate radiolabeled fatty acids in LDs, cells were treated for 4 hours with 1 µCi/ml of [^{14}C]-OA 175 µg/ml (NEC317050C, PerkinElmer, Waltham, Massachussetts). The media was then replaced with fresh media at 175 µg/ml of OA for an additional 4 hours followed by an overnight incubation with DMEM 0% FCS, low glucose (0.75 g per liter) with or without LPS (100 µg/ml) and sealed. Oxidation measurements were performed by trapping the released [^{14}C] carbon dioxide in a parafilm-sealed system on filter paper soaked in 1 M potassium hydroxide and measured using a Wallac 1409 Liquid Scintillation Counter. The rate of beta-oxidation was calculated as the amount of trapped [^{14}C] carbon dioxide in relative units produced per 0.5×10^6 cells. Results are expressed as the beta-oxidation rate relative to the untreated condition. Lipid soluble intermediates include those incompletely oxidized acid-soluble metabolites containing ^{14}C and were obtained after precipitation with perchloric acid and measured using a liquid scintillation counter.

Human macrophages studies

Cell culture

Human monocyte-derived macrophages (HMDMs) were obtained by differentiating CD14$^+$ monocytes as previously described (*37*). The human monocytic THP-1 cell line was obtained from the American Type Culture Collection (Rockville, Maryland). Cells were cultured in Roswell Park Memorial Institute 1640 Medium (RPMI, Gibco, ThermoFisher Scientific) containing 10% heat inactivated FBS (Bovogen Biologicals, Melbourne, VI, Australia), 5mM sodium pyruvate (Gibco), 10 mM HEPES (Gibco), 50 U/ml penicillin (Invitrogen, Carlsbad, California) and 50 µg/ml streptomycin (Invitrogen). Infection media are similar to complete media but without penicillin–streptomycin.

Bacterial strains and infection assays

For HMDMs infection, the following bacterial strains were used: *S.* Typhimurium SL1344 and *E. coli* K-12 MG1655. THP-1 cells were infected with *E. coli* K-12 MG1655. To induce LD formation, cells were treated with OA (178 µg/ml final) 18 hours prior infection. Bacterial infections were performed as previously described (*37*), with a multiplicity of infection (MOI) of 10 for *S.* Typhimurium and 100 for *E. coli*.

Flow cytometry

HMDMs were seeded at 0.5×10^6 cells/ml and treated with or without OA (178 ng/ml) for 16 hours. The next day, heat-killed pHrodoTM Green *E. coli* BioParticlesTM Conjugate (#P35366, ThermoFisher Scientific) were added to the well (50 µg/well) for 90 min. Cytochalasin D (10 µM, 30 min pre-treatment) was used as positive control to block phagocytosis (ThermoFisher Scientific). Cells were then harvested in ice-cold PBS containing 0.1% sodium azide and 25 mM EDTA. Flow cytometric analysis was performed using a GALLIOS Flow Cytometer (Beckman Coulter) and data were analyzed using Kaluza Analysis 1.3. software.

Fluorescence and quantitation of LD-bacteria proximity

HMDMs, plated on coverslips, were treated with OA (175 µg/ml) for 16 hours, then infected with *E. coli* strain MG1655 (MOI 10) or *Salmonella* SL1344 strain (MOI 10), both expressing mCherry constitutively. At 4 hours post-infection, cells were stained with BODIPY 647 (10 µg/ml; Molecular Probes Eugene, Oregon) for 30 min, before being washed with PBS and fixed with 4% paraformaldehyde (Electron Microscopy Science, Hatfield, Pennsylvania) for 10 min. Cells were then stained with 4′,6-diamidino-2-phenylindole (DAPI) (20 ng/ml) and mounted on slides.

HMDM siRNA experiments

Day 6 HMDMs were harvested and resuspended in IMDM complete media containing 10 mM HEPES buffer (pH 7.2 to 7.5, Gibco). Combined sets of CAMP small interfering RNA (siRNA) (GGAAGCUGUGCUUCGUGCUAUAGAU, AUCUAUAGCACGAAG CACAGCUUCC, GACAUCAGUUGUGAUAAGGAUAACA,

UGUUAUCCUUAUCAC AACUGAUGUC, GCUUCACAGUGAAAGAGACAGUGUG, and CACACUGUCUCCUUC ACUGUGAAGC) or scramble siRNA were used as previously described (*38*). After 24 hours recovery, cells were treated with OA (37.5 μg/ml) for another 18 hours. HMDMs were then infected with *E. coli*.

Gene overexpression in THP-1 by lentiviral transduction

Lentiviral transduction was used for gene overexpression of *PLIN5* in THP-1 cells as previously described (*38*).

Cell culture studies

Cell culture and treatments

HuH7 and HEK293 cells were cultured in Dulbecco's modified Eagle's medium (DMEM, Biological Industries, Cromwell, Connecticut) 10% v/v fetal bovine serum (Biological Industries) supplemented with 4 mM L-glutamine, 1 mM pyruvate (Sigma-Aldrich), 50 U/ml penicillin, 50 μg/ml streptomycin, and non-essential amino acids (Biological Industries). HEK293 cells stably expressing human Toll-like receptor 4 (HEK293-TLR4$^+$) have been characterized previously (*39*). OA treatments were performed using OA (O1008, Sigma-Aldrich) conjugated to fatty acid-free BSA (A8806, Sigma-Aldrich) at a molar ration of 6:1. Cells were treated with recombinant human TNFα (20 ng/ml; 300-01A, Preprotech, Rocky Hill, New Jersey), and IFNγ (10ng/ml; 300-02, Preprotech) and LPS (500 ng/ml) for 16 hours. Cells expressing CAMP-ΔN mutant were treated with MG132 (5 μM; 474790, Merck) for 24 hours.

Transfection

Six-well plates were seeded with 3×10^5 HuH7 cells or 4×10^5 HEK293 or HEK293-TLR4$^+$ cells. Twenty-four hours after plating, cells were transfected using GENEJET PLUS (SignaGen, Rockville, Maryland), following the manufacturer's instructions. Six hours after transfection, cells were treated with OA (175 μg/ml) for 16 hours.

Bacterial strains and infection assays

The bacterial strains used were: *E. coli* (ATCC 25922), MRSA (strain 162057-900), *P. aeruginosa* (ATCC 27853), and *L. monocytogenes* (strain 10403S). HEK293 or HEK293-TLR4$^+$ cells were seeded at 4×10^5 cells/plate in 6-well plates and transfected the next day. Six hours after transfection, culture media was replaced for antibiotic-free cell culture medium in presence of OA (175 μg/ml) and left overnight. Bacteria were grown overnight to stationary phase. The following day, bacteria were diluted 1:10 and grown to an O.D. at 600 nm of 0.54 to 0.56. They were then washed twice and resuspended in antibiotic-free cell culture medium and used at MOI of 0.5. Each infection was performed in triplicate wells. After 1 hour, extracellular bacteria were removed by incubation with 200 μg/ml gentamycin-containing medium (G1914, Sigma-Aldrich) for 1 hour, followed by incubation with 20 μg/ml gentamycin-containing medium for 4 hours. To determine intracellular bacterial loads, cells were lysed with 0.1% Triton X-100 (T8787, Sigma-Aldrich) for 5 min and plated onto LB medium supplemented with 1.5% (w/v) agar.

Cell fractionation

HuH7 cells were seeded at 1.5×10^6 cells/plate, transfected the next day and loaded with 175 μg/ml OA overnight. Three 100-mm culture plates were used per each condition. A sucrose density gradient was performed as previously described (*40*).

Protein purification and coimmunoprecipitation

For purification of myc-tagged proteins, HuH7 cells were plated in 100-mm culture plates at 10×10^6 cells/plate, transfected the next day and loaded with 175 μg /ml OA overnight. Myc-tagged proteins from the cellular extract and secreted into the media were purified using a c-myc protein purification kit (MBL, Nagoya, Japan) according to the manufacturer's instructions. Samples were processed by SDS–PAGE and analyzed by immunoblotting. For immunoprecipitation, transfected HuH7 cells (five 100-mm culture plates per condition) were collected and lysed in buffer containing 50 mM Tris-HCl at pH 7.5, 150 mM NaCl, 5 mM EDTA, and 1% Triton X-100 supplemented with proteases and phosphatases inhibitors. Cell lysates were homogenized with a 23G needle syringe 10 times and centrifuged for 20 min at 16,000*g* at 4°C. The supernatant was then incubated with 1 μg of anti- FLAG antibody for 2 hours at 4°C, followed by addition of protein G Sepharose beads (P3296, Sigma-Aldrich) for 1 hour at 4°C. Immunoprecipitated proteins were washed three times with lysis buffer, suspended in 2X Laemmli buffer and analyzed by immunoblotting.

Gene expression by quantitative PCR (qPCR)

For quantitative RT-PCR, total RNA was isolated from liver homogenates, HuH7 or HEK293-TLR4$^+$ cells using the RNeasy Lipid Tissue Mini Kit (QIAGEN, Hilden, Germany) according to the manufacturer's instructions. One microgram of total RNA was used for cDNA synthesis using the High Capacity cDNA Reverse Transcription Kit (Applied Bioscience, ThermoFisher Scientific) according to the manufacturer's instructions. qRT-PCR was performed using the Brilliant SYBR Green qPCR Master Mix (# 600548, Agilent Technologies, Santa Clara, California) and detected by the Mx3000P QPCR System (Agilent Technologies).

The following are the primers used for real-time PCR:

GAPDH: forward, 5′-CGACTTCAACAGCAACTCCCACTCTTCC-3′ and reverse 5′-TGGGTGGTCCAGGGTTTCTTACTCCTT-3′. Cytochrome C oxidase subunit I (*COI*): forward, 5′-GCCCCAGATATAGCATTCCC-3′ and reverse 5′-GTTCATCCTGTTCCTGCTCC-3′. *PLIN2*: forward 5′-ACACCCTCCTGTCCAACATC-3′ and reverse 5′-AAGGGACCTACCAGCCAGTT-3′. *PLIN5*: forward 5′-GCGGTCTGCGATGTTTACAG-3′ and reverse 5′-CTCCGAAGGTTGCTGGAGAA-3′. *RAB18*: forward 5′-GACGTGCTAACCACCCTGAA-3′ and reverse 5′-AACACCCTGTGCACCTCTAT-3′. *HSL*: forward 5′-CACCAGCCAACACTCAGCTA-3′ and reverse 5′-GTGTGAGGAGGGTCATCGTT-3′. *HPRT*: forward 5′-GCAGTACAGCCCCAAAATGG-3′ and reverse 5′-AACAAAGTCTGGCCTGTATCCAA-3′. *CAMP*: forward 5′-CTGTCCCCATACACCGCTTC-3′ and reverse 5′-GACACAGTGTGCCCCAGGAC-3′. *TNFα*: forward 5′-CCATGTTGTAGCAAACCCTCAA-3′ and reverse 5′-GCTGGTTATCTCTCAGCTCCA-3′. *IL8*: forward 5′-AGACAGCAGAGCACACAAGC-3′ and reverse 5′-ATGGTTCCTTCCGGTGGT-3′. *18 S:* forward 5′-CGGCTACCACATCCAAGGAA-3′ and reverse 5′-GCTGGAATTACCGCGGCT-3′. The relative expression of each mRNA was normalized to the internal reference *GAPDH* (liver), *18S* (cultured cells), or hypoxanthine phosphoribosyl transferase (*HPRT*; macrophages).

TLR4-mediated IL-8 release assay

HEK293-TLR4$^+$ cells were seeded at 4×10^5 cells/plate in 48-well plates in the presence or absence of LPS (250 ng/ml) for 18 hours. One hundred microliters of culture supernatant was used to measure interleukin-8 (IL-8) levels using the Human enzyme-linked immunosorbent assay (ELISA) IL-8 Set assay (555244; BD OptEIA, BD Biosciences) according to the manufacturer's protocol and detected by Epoch Multiplate Spectrophotometer (BioTek, Winooski, Vermont).

Immunofluorescence

HuH7 cells were grown in 10-mm glass coverslips. For HEK293 and HEK293-TLR4$^+$ cells, glass coverslips were coated with 50 μg/ml of fibronectin (Sigma-Aldrich) for 30 min at room temperature and rinsed twice with PBS before seeding cells. Cells were fixed for 60 min in 4% paraformaldehyde, permeabilized in 0.15% Triton X-100 for 10 min, followed by blocking with 1% BSA (A7906, Sigma-Aldrich), 0.1% Tween in PBS for 15 min. Labeling was achieved by incubating cells for 1 hour at room temperature with primary antibodies diluted in blocking solution: rabbit polyclonal anti-PLIN2 (1:500; ab108323, Abcam), rabbit polyclonal anti-CAMP (1:200; ab 180760, Abcam), rabbit polyclonal anti-TOM20 (1:500; ab186734, Abcam), mouse monoclonal anti-FLAG (1:500; F1804; Sigma). Primary antibodies were detected

with donkey anti-mouse IgG Alexa Fluor 488 (A21202), donkey anti-mouse IgG Alexa Fluor 555 (A31570), donkey anti-rabbit IgG Alexa Fluor 555 (A321094), and chicken anti-mouse IgG Alexa Fluor 647 (A21463) from ThermoFisher Scientific, diluted 1:250 in blocking solution. Finally, cells were labeled with DAPI (1:4000; ThermoFisher) and LDs were stained with BODIPY 493/503 (1:1000; Molecular Probes) for 10 min at room temperature, washed twice with PBS and coverslips were mounted with Mowiol (475904; Calbiochem, Merck). Alternatively, LDs were labeled with LipidTOX Deep Red (H34477; Molecular Probes) at 1:100 dilution in mounting media.

Microscopy

Optical and fluorescence microscopy

Imaging of H&E staining was performed with a Leica DMRB optical microscope (Leica, Wetzlar, Germany) equipped with a Leica DFC450 digital camera, using the 63X oil immersion objective lens. For immunohistochemistry and immunofluorescence, images were collected using a Leica AF600 motorized microscopy system (Leica Microsystems, Manheim, Germany) equipped with a DMI6000 microscope, a Leica PL APO 63X numerical aperture 1.4 oil immersion, a high-resolution monochrome ORCA-spark CMOS Digital Camera, and a mercury metal halide bulb Leica EL6000 as light source. DAPI was acquired with a band pass excitation filter 340-380 nm, dichromatic mirror (400 nm) and a long pass emission filter (425 nm). A488 was acquired with a band excitation filter 480/40 nm, dichromatic mirror 505 nm and a band pass emission filter (527/30 nm). A555 was acquired with a band pass excitation filter 531/40 nm, dichromatic mirror reflection 499-555 and transmission 659-730 nm and a band pass emission filter (593/40 nm). A647 was acquired with excitation band pass filter 628/40 nm, dichromatic mirror reflection 549-651 nm and transmission 699-726 nm and a band pass emission filter (692/40 nm). Images were collected using the LAS X Navigator software. High-resolution images of liver areas were captured using the Tile Scan acquisition mode. For quantitation of LD-bacteria proximity, images were taken with 63X objective lens using a Zeiss Axiovert 200 Upright Microscope Stand with LSM 710 Meta Confocal Scanner, with spectral detection and Airyscan super resolution detector. Two-photon imaging with a fully tunable Mai Tai eHP DeepSee 760-1040nm laser (Zeiss, Oberkochen, Germany). Images were analyzed using the Adobe Photoshop CS3 software (Adobe Systems Inc. San Jose, California) and ImageJ (NIH).

Electron microscopy and morphological measurements

Liver samples, HMDMs, or THP-1 cells in 3-cm dishes were processed for TEM as described previously (*41*). For TEM, ultrathin sections (60 nm) were cut using an ultramicrotome (EM U26, Leica, Germany) and collected on copper mesh grids. Imaging was conducted on a Hitachi 7700 (Tokyo, Japan) at 80 kV. For serial block-face scanning electron microscopy (SBF-SEM), the stub was transferred to a Zeiss Sigma scanning electron microscope fitted with a Gatan 3view. Sectioning and imaging were conducted at 50-nm intervals with a voxel size of 11.5 by 11.5 nm, allowing for a field of view of 46 by 46 μm. Data obtained from SBF-SEM were analyzed using Imod software (*42*). Image stacks were aligned manually using the Midas command. Structures of interest were then segmented using the manual drawing tool aided by an automated interpolator tool. A mesh was placed on the objects allowing then to be viewed in three dimensions.

Image analysis

Image analysis was performed using FIJI-Image J (Wayne Rasband, NIH) (*43*, *44*). Custom-made macros were programmed with instructions for the automated image analysis pipelines.

LD-mitochondria contacts

Confocal images from fluorescently labeled HEK293 cells, Mitochondria (TOM20), LD (BODIPY), PLIN5 and nuclei (DAPI), were acquired to analyze contacts between mitochondria and LD under LPS and PLIN5 expression (fig. S7). Briefly, cells were segmented, individualized, and stored as Regions of Interest (ROI). LD segmentation was achieved through a Trainable Weka Segmentation classifier (*45*) on LD (BODIPY) channel image and mitochondria were segmented by intensity thresholding (autothreshold method "Otsu"). Contact regions between mitochondria and LD were first obtained by using the Colocalization Highlighter plugin (Pierre Bourdoncle, Institut Jacques Monod, Service Imagerie, Paris) and converted to a contour line section by skeletonization. Contact length and contact counts were quantified from each cell and stored in the results table. Mean PLIN5 intensity was quantified from each cell to differentiate expressing PLIN5 cells. The computer code is available at https://zenodo.org/badge/latestdoi/280189667.

Distribution of selected tagged human LD-proteins

To analyze distribution of selected tagged human LD-proteins in HuH7 cells, confocal *z*-sections from cells labeled with DAPI, anti-FLAG antibodies, anti-PLIN2 antibodies, and LipidTox were acquired. Briefly, cells were defined manually and LD-intensity thresholded. They were then converted to binary images stored in ROI Manager. The sum of intensities from anti-FLAG or anti-PLIN2 from LD ROIs was divided by the sum of intensities of anti-FLAG or anti-PLIN2 from each cell, multiplied by 100 and expressed as percentage of anti-FLAG or anti-PLIN2 protein on LDs respectively. LDs that contained at least one pixel of anti-FLAG or anti-PLIN2 labeling were counted as positive LDs for that labeling. The total counts of positive LDs for anti-FLAG or anti-PLIN2 was divided by the total amount of LDs and expressed as a percentage. The computer code is available at https://zenodo.org/badge/latestdoi/280200243.

Immunoblotting

Cells were washed twice with cold PBS before being scraped into ice-cold 10 mM Tris, pH 7.5, 150 mM NaCl, 5 mM EDTA 0.1% Triton X-100 and a mixture of protease and phosphatase inhibitors. Cells were homogenized by sonication at 4°C. Protein was quantified with the Bio-Rad Protein Assay kit (Bio-Rad, Hercules, California). Immunoblotting of cells was performed as described previously (*46*). The blots were incubated with primary antibodies for 1 hour at room temperature. The primary antibodies used were: rabbit polyclonal anti-GFP (1:5000; ab290, Abcam), rabbit polyclonal anti-PLIN2 (1:5000; ab78920, Abcam), rabbit polyclonal anti- PLIN5 (1:1000; ab222811, Abcam), rabbit polyclonal anti-EEA1 (1:200; ab2900, Abcam), rabbit polyclonal anti-VAP-A (1:5000; ab181067, Abcam), mouse monoclonal anti-viperin (1:1000; ab107359, Abcam), rabbit polyclonal anti-CAMP (1:1000; ab180760, Abcam), guinea pig polyclonal anti-PLIN 3 (1:500; GP32, Progen, Heidelberg, Germany), guinea pig polyclonal PLIN5 (1:1000; GP31, Progen), guinea pig polyclonal PLIN2 (1:2000; GP41, Progen), mouse monoclonal anti-GM130 (1:2000; Labs 810822,BD-Biosciences San Jose, California), mouse monoclonal anti-Na/K ATPase (1:1000; 05-369 Upstate-Millipore, Darmstadt, Germany) rabbit polyclonal anti-HSL (1:1000; 4107, Cell Signaling, Leiden, the Netherlands), mouse monoclonal anti- IGTP (1:200; sc-136317, Santa Cruz Biotechnology, Dallas, Texas), rabbit polyclonal anti-CAMP (1:500; TA306515, OriGene), mouse monoclonal anti-FLAG (1:1000; F1804, Sigma-Aldrich), mouse monoclonal anti-ATP synthase (1:500; 7H10BD4F9, ThermoFisher Scientific), and goat polyclonal anti-GAPDH (1:5000; A00191, GenScript). After incubation with primary antibodies, membranes were washed and incubated with the following peroxidase-conjugated secondary antibodies (1:3000): goat anti-rabbit IgG (H+L)–HRP conjugate (1706515, BioRad), goat anti-mouse IgG (H+L)-HRP conjugate (1706516, BioRad), and peroxidase AffiniPure donkey anti-goat IgG (H+L) (705-035-147, Jackson ImmunoResearch, Ely, UK). HRP-conjugated secondary antibodies were detected with ECL (Biological Industries) and visualized using ImageQuant LAS4000 (GE Healthcare, Chicago, Illinois). Immunoblots were quantified using the Fiji-ImageJ software (NIH).

Quantitative proteomics and functional annotation analyses

Proteins were precipitated from either isolated lipid droplets (four and five independent replicates for CTL- and LPS-treated, respectively) or liver homogenates (three independent replicates per condition) with ice-cold acetone and solubilized in lysis buffer (50 mM Tris-HCl, pH 7.5, 2% SDS and 10 mM TCEP [Tris-(2-carboxyethyl)-phosphine hydrochloride]. Protein concentration in spun supernatants was determined by infrared spectrometry. Approximately 100 μg of total protein per sample were digested using standard FASP procedures. After alkylation, proteins were digested overnight at 37°C with modified trypsin (Promega) in 50 mM ammonium bicarbonate at a 30:1 protein:trypsin (w/w) ratio. Resulting peptides were eluted in 50 mM ammonium bicarbonate and 0.5 M sodium chloride. Trifluoroacetic acid (TFA) was added to a final concentration of 1%. Eluates were desalted through C18 Oasis-HLB cartridges (Waters corporation, Milford, Massachussetts), dried, and resuspended in 100 mM triethylammonium bicarbonate (TEAB) buffer. Equal amounts of each peptide sample were labeled using the 10-plex TMT Reagents (ThermoFisher Scientific) according to manufacturer's protocol. For increased proteome coverage, TMT-labeled samples were fractionated by high-pH reverse-phase chromatography (Pierce High pH Reversed-Phase Peptide Fractionation Kit, # 84868; ThermoFisher Scientific). Labeled peptides were chromatographed through a C-18 reversed phase nano-column (75 μm I.D. × 50 cm, 2-μm particle size, Acclaim PepMap RSLC, 100 C18; ThermoFisher Scientific) in a continuous acetonitrile gradient consisting of 0 to 30% B in 360 min, 50 to 90% B in 3 min (A = 0.1% formic acid; B = 90% acetonitrile, 0.1% formic acid; flow rate of 200 nl/min) for analysis in an Orbitrap Fusion mass spectrometer (ThermoFisher Scientific). Tandem mass spectrometry (MS/MS) spectra from the Nth-most intense parent ions were analyzed along the chromatographic run. For peptide identification, all spectra were analyzed with Proteome Discoverer (v. 2.1.0.81) using SEQUEST-HT (ThermoFisher Scientific) and queried onto the Uniprot database with the following search parameters: 2 maximum missed tryptic sites; precursor and fragment mass tolerances of 2 Da and 0.02 Da, respectively; carbamidomethyl cysteine and TMT modifications at N-terminal and Lys residues as fixed modifications, and methionine oxidation as dynamic modification. Peptide identification was performed using the probability ratio method (*47*), and FDR was calculated using inverted databases. The relative abundance of each protein was estimated from ion intensities of peptides with an FDR ≤ 1% and expressed in units of standard deviation according to their estimated variances (*Zq* values), as previously described (*13*). Hierarchical clustering was computed across all individual replicates (averaged distance) and a 0.78 correlation cut-off was established for subsequent analysis. Functional protein analysis was performed using the system biology triangle (SBT) algorithm and Ingenuity Pathway Analysis (IPA, QIAGEN) (*48*). Upstream pathway analysis and network modeling of interested protein clusters were run using the IPA platform (QIAGEN), and network representation was layered out using Cytoscape 2.0. Analysis shown in Fig. 3C shows the relative proportion of proteins identified for each indicated functional annotation term (retrieved from DAVID resource 6.7, including all KEGG and GO terms), from either mitochondrial protein identified among LPS-LD down-regulated proteins, or the MitoCarta 2.0 reference proteome. Mass spectrometry data have been deposited in Peptide Atlas (ID: PASS01610).

Statistical analysis

All data shown in graphs are the mean ± SD. Statistical significance was determined using paired *t* test, one-way analysis of variance (ANOVA) multiple comparisons test, or two-sided students *z* test on proportions, as specified in figure legends [not significant (ns), $*P < 0.05$, $**P < 0.01$, $***P < 0.001$, and $****P < 0.0001$].

Figure preparation

Figures were created using Microsoft PowerPoint (Microsoft 365 MSO). Images were edited with Adobe Photoshop CS3 software (Adobe Systems). GraphPad Prism 7 (GraphPad Software) was used to create graphs and calculate statistical significances.

REFERENCES AND NOTES

1. A. Pol, S. P. Gross, R. G. Parton, Review: Biogenesis of the multifunctional lipid droplet: lipids, proteins, and sites. *J. Cell Biol.* **204**, 635–646 (2014). doi: 10.1083/jcb.201311051; pmid: 24590170
2. A. L. Vallochi, L. Teixeira, K. D. S. Oliveira, C. M. Maya-Monteiro, P. T. Bozza, Lipid Droplet, a key player in host-parasite interactions. *Front. Immunol.* **9**, 1022 (2018). doi: 10.3389/fimmu.2018.01022; pmid: 29875768
3. P. Roingeard, R. C. Melo, *Cell. Microbiol.* 10.1111/cmi.12688 (2017).
4. M. Knight, J. Braverman, K. Asfaha, K. Gronert, S. Stanley, Lipid droplet formation in Mycobacterium tuberculosis infected macrophages requires IFN-γ/HIF-1α signaling and supports host defense. *PLOS Pathog.* **14**, e1006874 (2018). doi: 10.1371/journal.ppat.1006874; pmid: 29370315
5. R. C. Melo, A. M. Dvorak, Lipid body-phagosome interaction in macrophages during infectious diseases: Host defense or pathogen survival strategy? *PLOS Pathog.* **8**, e1002729 (2012). doi: 10.1371/journal.ppat.1002729; pmid: 22792061
6. E. R. Hinson, P. Cresswell, The antiviral protein, viperin, localizes to lipid droplets via its N-terminal amphipathic alpha-helix. *Proc. Natl. Acad. Sci. U.S.A.* **106**, 20452–20457 (2009). doi: 10.1073/pnas.0911679106; pmid: 19920176
7. L. Bougnères *et al.*, A role for lipid bodies in the cross-presentation of phagocytosed antigens by MHC class I in dendritic cells. *Immunity* **31**, 232–244 (2009). doi: 10.1016/j.immuni.2009.06.022; pmid: 19699172
8. P. Anand *et al.*, A novel role for lipid droplets in the organismal antibacterial response. *eLife* **1**, e00003 (2012). doi: 10.7554/eLife.00003; pmid: 23150794
9. U. Protzer, M. K. Maini, P. A. Knolle, Living in the liver: Hepatic infections. *Nat. Rev. Immunol.* **12**, 201–213 (2012). doi: 10.1038/nri3169; pmid: 22362353
10. J. C. Kagan, Lipopolysaccharide Detection across the Kingdoms of Life. *Trends Immunol.* **38**, 696–704 (2017). doi: 10.1016/j.it.2017.05.001; pmid: 28551077
11. A. Herms *et al.*, AMPK activation promotes lipid droplet dispersion on detyrosinated microtubules to increase mitochondrial fatty acid oxidation. *Nat. Commun.* **6**, 7176 (2015). doi: 10.1038/ncomms8176; pmid: 26013497
12. J. Behnsen, A. Perez-Lopez, S. P. Nuccio, M. Raffatellu, Exploiting host immunity: The Salmonella paradigm. *Trends Immunol.* **36**, 112–120 (2015). doi: 10.1016/j.it.2014.12.003; pmid: 25582038
13. P. Navarro *et al.*, General statistical framework for quantitative proteomics by stable isotope labeling. *J. Proteome Res.* **13**, 1234–1247 (2014). doi: 10.1021/pr4006958; pmid: 24512137
14. N. Krahmer *et al.*, Protein correlation profiles identify lipid droplet proteins with high confidence. *Mol. Cell. Proteomics* **12**, 1115–1126 (2013). doi: 10.1074/mcp.M112.020230; pmid: 23319140
15. K. Bersuker *et al.*, A proximity labeling strategy provides insights into the composition and dynamics of lipid droplet proteomes. *Dev. Cell* **44**, 97–112.e7 (2018). doi: 10.1016/j.devcel.2017.11.020; pmid: 29275994
16. E. L. Mills, B. Kelly, L. A. J. O'Neill, Mitochondria are the powerhouses of immunity. *Nat. Immunol.* **18**, 488–498 (2017). doi: 10.1038/ni.3704; pmid: 28418387
17. M. Bosch, R. G. Parton, A. Pol, *Semin. Cell Dev. Biol.* 10.1016/j.semcdb.2020.02.010 (2020).
18. H. A. Neufeld, J. A. Pace, F. E. White, The effect of bacterial infections on ketone concentrations in rat liver and blood and on free fatty acid concentrations in rat blood. *Metabolism* **25**, 877–884 (1976). doi: 10.1016/0026-0495(76)90120-7; pmid: 181658
19. A. Fabisiak, N. Murawska, J. Fichna, LL-37: Cathelicidin-related antimicrobial peptide with pleiotropic activity. *Pharmacol. Rep.* **68**, 802–808 (2016). doi: 10.1016/j.pharep.2016.03.015; pmid: 27117377
20. X. Shu, L. Nelbach, R. O. Ryan, T. M. Forte, Apolipoprotein A-V associates with intrahepatic lipid droplets and influences triglyceride accumulation. *Biochim. Biophys. Acta* **1801**, 605–608 (2010). doi: 10.1016/j.bbalip.2010.02.004; pmid: 20153840
21. S. Turró *et al.*, Identification and characterization of associated with lipid droplet protein 1: A novel membrane-associated protein that resides on hepatic lipid droplets. *Traffic* **7**, 1254–1269 (2006). doi: 10.1111/j.1600-0854.2006.00465.x; pmid: 17004324
22. C. L. Libbing, A. R. McDevitt, R. P. Azcueta, A. Ahila, M. Mulye, Lipid droplets: A significant but understudied contributor of host bacterial interactions. *Cells* **8**, 354 (2019). doi: 10.3390/cells8040354; pmid: 30991653
23. J. L. Cocchiaro, Y. Kumar, E. R. Fischer, T. Hackstadt, R. H. Valdivia, Cytoplasmic lipid droplets are translocated into the lumen of the *Chlamydia trachomatis* parasitophorous vacuole. *Proc. Natl. Acad. Sci. U.S.A.* **105**, 9379–9384 (2008). doi: 10.1073/pnas.0712241105; pmid: 18591669
24. P. Peyron *et al.*, Foamy macrophages from tuberculous patients' granulomas constitute a nutrient-rich reservoir for M. tuberculosis persistence. *PLOS Pathog.* **4**, e1000204 (2008). doi: 10.1371/journal.ppat.1000204; pmid: 19002241
25. K. A. Mattos *et al.*, Modulation of lipid droplets by Mycobacterium leprae in Schwann cells: A putative mechanism for host lipid acquisition and bacterial survival in phagosomes. *Cell. Microbiol.* **13**, 259–273 (2011). doi: 10.1111/j.1462-5822.2010.01533.x; pmid: 20955239
26. S. J. Nolan, J. D. Romano, I. Coppens, Host lipid droplets: An important source of lipids salvaged by the intracellular parasite *Toxoplasma gondii*. *PLOS Pathog.* **13**, e1006362 (2017). doi: 10.1371/journal.ppat.1006362; pmid: 28570716
27. J. S. Mader, N. Mookherjee, R. E. Hancock, R. C. Bleackley, The human host defense peptide LL-37 induces apoptosis in a calpain- and apoptosis-inducing factor-dependent manner involving Bax activity. *Mol. Cancer Res.* **7**, 689–702 (2009). doi: 10.1158/1541-7786.MCR-08-0274; pmid: 19435812
28. S. N. Keenan *et al.*, Perilipin 5 deletion in hepatocytes remodels lipid metabolism and causes hepatic insulin resistance in mice. *Diabetes* **68**, 543–555 (2019). doi: 10.2337/db18-0670; pmid: 30617219
29. D. J. Greenwood *et al.*, Subcellular antibiotic visualization reveals a dynamic drug reservoir in infected macrophages. *Science* **364**, 1279–1282 (2019). doi: 10.1126/science.aat9689; pmid: 31249058
30. R. Dubey *et al.*, Lipid droplets can promote drug accumulation and activation. *Nat. Chem. Biol.* **16**, 206–213 (2020). doi: 10.1038/s41589-019-0447-7; pmid: 31932720

31. D. M. Moujalled *et al*., TNF can activate RIPK3 and cause programmed necrosis in the absence of RIPK1. *Cell Death Dis.* **4**, e465 (2013). doi: 10.1038/cddis.2012.201; pmid: 23328672
32. J. M. Murphy *et al*., The pseudokinase MLKL mediates necroptosis via a molecular switch mechanism. *Immunity* **39**, 443–453 (2013). doi: 10.1016/j.immuni.2013.06.018; pmid: 24012422
33. M. Bosch *et al*., Hepatic primary and secondary cholesterol deposition and damage in niemann-pick disease. *Am. J. Pathol.* **186**, 517–523 (2016). doi: 10.1016/j.ajpath.2015.12.002; pmid: 26784526
34. A. Tutusaus *et al*., A functional role of GAS6/TAM in nonalcoholic steatohepatitis progression implicates AXL as therapeutic target. *Cell. Mol. Gastroenterol. Hepatol.* **9**, 349–368 (2020). doi: 10.1016/j.jcmgh.2019.10.010; pmid: 31689560
35. A. Barrientos, In vivo and in organello assessment of OXPHOS activities. *Methods* **26**, 307–316 (2002). doi: 10.1016/S1046-2023(02)00036-1; pmid: 12054921
36. M. Bosch *et al*., Caveolin-1 deficiency causes cholesterol-dependent mitochondrial dysfunction and apoptotic susceptibility. *Curr. Biol.* **21**, 681–686 (2011). doi: 10.1016/j.cub.2011.03.030; pmid: 21497090
37. R. Kapetanovic *et al*., *Salmonella* employs multiple mechanisms to subvert the TLR-inducible zinc-mediated antimicrobial response of human macrophages. *FASEB J.* **30**, 1901–1912 (2016). doi: 10.1096/fj.201500061; pmid: 26839376
38. C. J. Stocks *et al*., *J. Leukoc. Biol.* **2020**, 1–11 (2020).
39. S. Lauer, Y. A. Kunde, T. A. Apodaca, B. Goldstein, E. Hong-Geller, Soluble MD2 increases TLR4 levels on the epithelial cell surface. *Cell. Immunol.* **255**, 8–16 (2009). doi: 10.1016/j.cellimm.2008.08.009; pmid: 18845299
40. A. Kassan *et al*., Acyl-CoA synthetase 3 promotes lipid droplet biogenesis in ER microdomains. *J. Cell Biol.* **203**, 985–1001 (2013). doi: 10.1083/jcb.201305142; pmid: 24368806
41. A. Herms *et al*., Cell-to-cell heterogeneity in lipid droplets suggests a mechanism to reduce lipotoxicity. *Curr. Biol.* **23**, 1489–1496 (2013). doi: 10.1016/j.cub.2013.06.032; pmid: 23871243
42. J. R. Kremer, D. N. Mastronarde, J. R. McIntosh, Computer visualization of three-dimensional image data using IMOD. *J. Struct. Biol.* **116**, 71–76 (1996). doi: 10.1006/jsbi.1996.0013; pmid: 8742726
43. J. Schindelin *et al*., Fiji: An open-source platform for biological-image analysis. *Nat. Methods* **9**, 676–682 (2012). doi: 10.1038/nmeth.2019; pmid: 22743772
44. C. A. Schneider, W. S. Rasband, K. W. Eliceiri, NIH Image to ImageJ: 25 years of image analysis. *Nat. Methods* **9**, 671–675 (2012). doi: 10.1038/nmeth.2089; pmid: 22930834
45. I. Arganda-Carreras *et al*., Trainable Weka Segmentation: A machine learning tool for microscopy pixel classification. *Bioinformatics* **33**, 2424–2426 (2017). doi: 10.1093/bioinformatics/btx180; pmid: 28369169
46. A. Pol, D. Ortega, C. Enrich, Identification and distribution of proteins in isolated endosomal fractions of rat liver: Involvement in endocytosis, recycling and transcytosis. *Biochem. J.* **323**, 435–443 (1997). doi: 10.1042/bj3230435; pmid: 9163335
47. S. Martínez-Bartolomé *et al*., Properties of average score distributions of SEQUEST: The probability ratio method. *Mol. Cell. Proteomics* **7**, 1135–1145 (2008). doi: 10.1074/mcp.M700239-MCP200; pmid: 18303013
48. F. García-Marqués *et al*., A novel systems-biology algorithm for the analysis of coordinated protein responses using quantitative proteomics. *Mol. Cell. Proteomics* **15**, 1740–1760 (2016). doi: 10.1074/mcp.M115.055905; pmid: 26893027

ACKNOWLEDGMENTS

We thank M. Calvo and G. Martín and acknowledge the use of the Advanced Optical Microscopy Facility of the University of Barcelona. We are indebted to C. Ferguson and J. Rae and acknowledge the use of the Australian Microscopy and Microanalysis Research Facility at the Center for Microscopy and Microanalysis at The University of Queensland. We thank J. Murphy (Walter and Elizabeth Hall Institute of Medical Research, Melbourne, Australia) for providing the pF_TRE3G_PGK_puro construct. We are indebted to the Protein Expression Facility (University of Queensland) for valuable assistance. We thank the Australian Red Cross Blood Service for providing buffy coats for the isolation of human monocytes. Last, we are indebted to the Citomics unit of IDIBAPS for their technical help. **Funding:** M.B. acknowledges support from 31/U/2016 from Fundació Marató de TV3. R.K. acknowledges support from an Australian Research Council Discovery Early Career Research Award (DE130100470). B.S. is supported by an Early Postdoc Mobility fellowship from the Swiss National Science Foundation (P2ZHP3_184024). M.J.S. is supported by a National Health and Medical Research Council (NHMRC) Senior Research Fellowship (APP1107914). M.S.-A. was recipient of a CNIC IPP fellowship (COFUND 2014). M.M. is supported by the Instituto de Salud Carlos III (FIS PI19/01410). O.T. is founded by Amgen 2018 Competitive Grant Program. A.P., R.G.P., S.P.G., and P.T.B. have been supported by RGP0020/2015 from the Human Frontier Science Program (HFSP). A.P. is supported by the Ministerio de Ciencia e Innovación (MICINN, RTI2018-098593-B-I00), Fundació Marató de TV3 (31/U/2016), and the CERCA Programme/Generalitat de Catalunya. R.G.P. was supported by the NHMRC of Australia (program grant APP1037320 and Senior Principal Research Fellowship 569452), and the Australian Research Council Centre of Excellence in Convergent Bio-Nanoscience and Technology (CE140100036). P.T.B. is supported by Conselho Nacional de Desenvolvimento Científico e Tecnológico (CNPq) of Brazil and Fundaçao de Amparo a Pesquisa do Estado do Rio de Janeiro (FAPERJ). M.A.D.P. was funded by MICINN (project grants SAF2014-51876-R and SAF2017-83130-R; and IGP-SO grant MINSEV1512-07-2016) and was a Worldwide Cancer Research Foundation grantee (#15-0404). J.V. is supported by MICINN (BIO2015-67580-P) and from the Carlos III Institute of Health-Fondo de Investigación Sanitaria (PRB2, IPT13/0001—ISCIII-SGEFI/FEDER, ProteoRed). The CNIC is supported by the MICINN and the Pro-CNIC Foundation and is a Severo Ochoa Center of Excellence (MICINN award SEV-2015-0505). **Author contributions:** M.B. and M.S.-A. contributed equally. Conceptualization: M.B., P.T.B., S.P.G., R.G.P., and A.P. Methodology: M.B., M.S.-A., and A.F. Formal analysis: M.B., R.G.P., and A.P. Investigation: M.B., M.S.-A., A.F., R.K., B.S., F.D., L.M., M.M., F.M.-P., O.T., A.G., R.M.T., J.E.B.C., C.C., N.M., J.A.L., R.C., and F.T. Resources and supervision: F.L., C.E., M.A.D.P., M.J.S., J.V., P.T.B., S.P.G., R.G.P., and A.P. Data curation: M.B., M.S.-A., F.T., R.G.P., and A.P. Writing (original draft): R.G.P. and A.P. Writing (review and editing): M.B., M.S.-A., M.S., P.T.B., S.P.G., R.G.P., and A.P. Visualization: R.G.P. and A.P. Project administration: P.T.B., S.P.G., R.G.P., and A.P. Funding acquisition: P.T.B., S.P.G., R.G.P., and A.P. **Competing interests:** None declared. **Data and materials availability:** Mass spectrometry data have been deposited in Peptide Atlas (ID: PASS01610). Computer code#1 to measure LD–mitochondria contacts can be found at https://zenodo.org/badge/latestdoi/280189667. Computer code#2 to quantify distribution of LD proteins can be found in: https://zenodo.org/badge/latestdoi/280200243. All other data are available in the main text or the supplementary materials.

SUPPLEMENTARY MATERIALS

science.sciencemag.org/content/370/6514/eaay8085/suppl/DC1
Materials and Methods
Figs. S1 to S12
Tables S1 to S7

View/request a protocol for this paper from *Bio-protocol*.

19 July 2019; resubmitted 29 April 2020
Accepted 21 August 2020
10.1126/science.aay8085

Mammalian lipid droplets are innate immune hubs integrating cell metabolism and host defense

Marta Bosch, Miguel Sánchez-Álvarez, Alba Fajardo, Ronan Kapetanovic, Bernhard Steiner, Filipe Dutra, Luciana Moreira, Juan Antonio López, Rocío Campo, Montserrat Marí, Frederic Morales-Paytuví, Olivia Tort, Albert Gubern, Rachel M. Templin, James E. B. Curson, Nick Martel, Cristina Català, Francisco Lozano, Francesc Tebar, Carlos Enrich, Jesús Vázquez, Miguel A. Del Pozo, Matthew J. Sweet, Patricia T. Bozza, Steven P. Gross, Robert G. Parton and Albert Pol

Science **370** (6514), eaay8085.
DOI: 10.1126/science.aay8085

Cells drop a bomb on pathogens

Lipid droplets (LDs) accumulate in cells to serve as lipid storage organelles. They are also an attractive source of nutrients for many pathogens. Bosch *et al.* show that various proteins involved in innate immunity form complexes on LDs in response to bacterial lipopolysaccharide (see the Perspective by Green). Upon activation, LDs became physically uncoupled from mitochondria, driving a shift in cells from oxidative phosphorylation to aerobic glycolysis. This work highlights the ability of LDs both to kill pathogens directly and to establish a metabolic environment conducive to host defense. This may inform future antimicrobial strategies in the age of antibiotic resistance.

Science, this issue p. eaay8085; see also p. 294